

# The Kinetics of H<sub>2</sub>O Vapor Condensation and Evaporation on Different Types of Ice in the Range 130–210 K<sup>†</sup>

Pascal Pratte, Hubert van den Bergh, and Michel J. Rossi\*

Ecole Polytechnique Fédérale de Lausanne (EPFL), Laboratoire de Pollution Atmosphérique et sol (LPAS), Bât CH H5, station 6, CH-1015 Lausanne, Switzerland

Received: July 19, 2005; In Final Form: September 8, 2005

The kinetics of condensation ( $k_c$ ) and the evaporation flux ( $J_{ev}$ ) of H<sub>2</sub>O on ice were studied in the range 130–210 K using pulsed-valve and steady-state techniques in a low-pressure flow reactor. The uptake coefficient  $\gamma$  was measured for different types of ice, namely, condensed (C), bulk (B), single crystal (SC), snow (S), and cubic ice (K). The negative temperature dependence of  $\gamma$  for C, B, SC, and S ice reveals a precursor-mediated adsorption/desorption process in agreement with the proposal of Davy and Somorjai.<sup>1</sup> The non-Arrhenius behavior of the rate of condensation,  $k_c$ , manifests itself in a discontinuity in the range 170–190 K depending on the type of ice and is consistent with the precursor model. The average of the energy of sublimation  $\Delta H_s^\circ$  is  $(12.0 \pm 1.4)$  kcal/mol for C, B, S, and SC ice and is identical within experimental uncertainty between 136 and 210 K. The same is true for the entropy of sublimation  $\Delta S_s$ . In contrast, both  $\gamma$  and the evaporative flux  $J_{ev}$  are significantly different for different ices. In the range 130–210 K,  $J_{ev}$  of H<sub>2</sub>O ice was significantly smaller than the maximum theoretically allowed value. This corroborates  $\gamma$  values significantly smaller than unity in that  $T$  range. On the basis of the present kinetic parameters, the time to complete evaporation of a small ice particle of radius 1  $\mu\text{m}$  is approximately a factor of 5 larger than that previously thought.

## 1. Introduction

Although only  $10^{-5}$  of the global abundance of H<sub>2</sub>O is present in the atmosphere, it is the most important greenhouse gas that primarily controls the global radiation budget on our planet. Owing in a large part to the positive radiative forcing of water vapor (H<sub>2</sub>O(g)) the greenhouse effect keeps the average global temperature well over the melting point of H<sub>2</sub>O and thus enables life on earth. Evaporation from oceans, lakes, and rivers is balanced by precipitation over land and sea leading to an average residence time of 10 days for H<sub>2</sub>O(g) in the atmosphere.<sup>2</sup> This means that the mixing of H<sub>2</sub>O vapor on a global scale is incomplete which leads to a large degree of spatial inhomogeneity of atmospheric H<sub>2</sub>O(g) and consequently to a high local variability of H<sub>2</sub>O(g).<sup>3–5</sup> It has been known for some time that a significant fraction of the free troposphere is either under- or supersaturated with respect to H<sub>2</sub>O(g) depending on meteorological conditions or long-range transport phenomena.<sup>4,6–8</sup> This fact and the large temperature fluctuations that accompany the “weather” in the free troposphere underline the importance of H<sub>2</sub>O(g) evaporation and condensation processes in the atmosphere both of which tend to restore thermodynamic equilibrium of H<sub>2</sub>O(g).

The present work focuses on the kinetics of condensation and evaporation of H<sub>2</sub>O on ice at low temperatures characteristic of the tropopause region, that is, in the upper troposphere (UT) and lower stratosphere (LS). Ice occurs as cirrus cloud or aviation contrail particles which have a positive radiative forcing leading to global warming in contrast to warm clouds at lower altitudes that mostly consist of liquid water droplets and that are approximately neutral with respect to global radiative

forcing.<sup>9</sup> Approximately a quarter of all cirrus clouds at any given time are visible by the naked eye because they have a significant optical thickness whereas the remaining 75% of the cirrus are subvisible.<sup>10</sup> The cirrus ice particles typically have radii of 10–20  $\mu\text{m}$ <sup>11–13</sup> in the tropical UT and often lead to local increases of positive radiative forcing.<sup>14</sup> Cirrus clouds are particularly prevalent in the cold tropical tropopause region to the extent of 50% of the atmosphere whereas their abundance decreases to approximately 25% at midlatitudes as indicated above.<sup>15</sup>

In addition to their known climate effect, these cirrus and contrail<sup>16</sup> ice particles also have an effect on the composition of the corresponding atmospheric strata as they not only support adsorption and desorption processes but may also contribute to the occurrence of heterogeneous chemical processes of atmospheric trace gases on ice. On the basis of a modeling study of heterogeneous chemistry in the midlatitude UT, a benchmark minimum reaction time of 20 min has been obtained that led to a significant perturbation of the UT composition.<sup>15,17</sup> This also means that a minimum ice particle lifetime of the same order had to be postulated, ice being the seat of the investigated heterogeneous processes. One of the most important ice particle characteristics is its evaporative lifetime in an atmosphere undersaturated with H<sub>2</sub>O(g) vapor which may be calculated at any relative humidity of H<sub>2</sub>O vapor if the basic chemical kinetics of equilibrium 1 involving the condensation rate constant ( $k_c/\text{s}^{-1}$ ) and the evaporation rate ( $R_{ev}/\text{molecules s}^{-1} \text{cm}^{-3}$ ) is known



If the uptake coefficient,  $\gamma$ , of H<sub>2</sub>O(g) on ice derived from  $k_c$  is assumed to be equal to unity, as has frequently been done, the cirrus ice particle lifetime is significantly less than 10 min at

<sup>†</sup> Part of the special issue “Jürgen Troe Festschrift”.

\* Corresponding author. E-mail: michel.rossi@epfl.ch.

temperatures ( $T$ ) and relative humidities of the UT; heterogeneous chemistry does not have a chance to occur under those conditions. Conversely, for  $\gamma$  significantly less than unity, as obtained in the present work, heterogeneous chemistry may perturb the atmospheric composition. Therefore, it is of utmost importance to obtain reliable kinetic parameters on both the rate constant of condensation ( $k_c$ ) and the rate of evaporation ( $F_{ev}/$  molecule  $s^{-1}$ ) as a function of temperature in the range of interest. The morphology of thermodynamically stable ice  $I_h$  may considerably vary depending on a suite of parameters that control the growth processes of atmospheric ice.<sup>18</sup> Although the above-mentioned kinetics may depend on the ice morphology, very little information from the field is available concerning the type of ice particles prevalent in cirrus clouds. Laboratory studies have revealed that liquid droplets frozen at  $T > 180$  K consist of  $I_h$ .<sup>19,20</sup> Recent laboratory reports even estimate the probability of finding metastable cubic ice ( $I_c$ ) in the atmosphere, whose occurrence has been suspected in the past.<sup>21–23</sup>

Because most of the literature reports the kinetics of H<sub>2</sub>O vapor with ice condensed from the vapor phase (condensed or C ice), the present work emphasizes this type of ice in order to provide a solid basis for quantitative comparison. The strategy adopted in the present work was to study the kinetics of H<sub>2</sub>O(g) condensation and evaporation on many different types of ices that we could generate in the laboratory under well-defined and reproducible conditions in order to learn more about the variability of the kinetic results as well as on the underpinning molecular mechanism. Several workers have oriented their efforts toward the measurement of the kinetics of H<sub>2</sub>O(g) both over liquid water and over ice in terms of  $\gamma$  as well as the evaporation rate  $R_{ev}$  or flux  $J_{ev}$  as a function of  $T$ .<sup>24–28</sup> Experimental values of  $\gamma$  range from 0.03 to 1.0 using different experimental techniques such as measurements of weight, ice crystal growth, droplet radial growth, vapor loss, liquid film growth, and IR absorption in the range 138–293 K.<sup>24–27,29–32</sup> The large variability in  $\gamma$  at any given temperature suggests the potential importance of controlling the many ice growth parameters in addition to allowing for potential experimental artifacts. We report the fundamental kinetics of the H<sub>2</sub>O(g) interaction with different types of ices generated in the laboratory under reproducible conditions using both pulsed valve in real-time as well as steady-state methods that enable the separate measurement of both the condensation and evaporation process displayed in reaction 1. The separate determination of both rates enabled the measurement of the equilibrium vapor pressure,  $P_{eq}$ , which serves as a powerful thermodynamic constraint for checking the internal consistency of the kinetics of the  $T$ -range of interest in thermochemical closure.

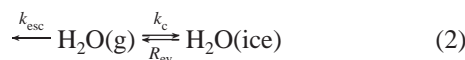
## 2. Experimental Setup

The experiments have been performed in a Teflon-coated Knudsen flow reactor equipped with molecular-beam-sampling electron-impact mass spectrometry (MS). A detailed description of this technique has been given elsewhere.<sup>33</sup> Two types of measurements have been performed: continuous flow and pulsed admission experiments (PV). The PV experiments correspond to a transient supersaturation of H<sub>2</sub>O(g) over ice using a pulsed solenoid valve through which short pulses of H<sub>2</sub>O molecules of several millisecond duration have been injected into the flow reactor. Each experiment has been performed in duplicate, that is a reference and a reactive experiment. The former yields the MS signal decay of H<sub>2</sub>O(g) when the sample compartment is isolated from the flow reactor, whereas the latter monitors the decay in the presence of the ice

**TABLE 1: Experimental Parameters**

reactor volume ( $V$ , cm <sup>3</sup> )	1830			
cryogenic sample surface ( $A_s$ , cm <sup>2</sup> )	17.65			
collision frequency of H <sub>2</sub> O on sample surface ( $\omega$ ) at 300 K (s <sup>-1</sup> )	143			
escape aperture diameter (mm)	14	8	4	1
escape rate constant (s <sup>-1</sup> )	$7.1 \pm 0.2$	$3.1 \pm 0.3$	$0.8 \pm 0.1$	$0.05 \pm 0.01$

substrate. The decay rate in the absence of the ice sample is given by the measured escape rate constant  $k_{esc}$  at which H<sub>2</sub>O(g) molecules effuse out of the reactor and is related to the gas-phase lifetime,  $\tau_g$ , of H<sub>2</sub>O(g) through the relation  $\tau_g = 1/k_{esc}$ . This represents the reference experiment against which the reactive decay of the MS signal in the presence of ice is measured. The measurement of  $k_{esc}$  was repeated 10 times for each orifice in order to obtain its standard deviation. The evaporation and condensation of H<sub>2</sub>O(g)/H<sub>2</sub>O(ice) on the ice substrate are competing with  $k_{esc}$  as displayed in reaction 2. In the presence of ice the measured pulse decay constant  $k_{dec}$  is the sum of the condensation  $k_c$  and escape rate constant  $k_{esc}$ , namely,  $k_{dec} = k_c + k_{esc}$ . From the measured decay constant  $k_{dec}$ ,  $k_c$  is directly accessible using the measured value of  $k_{esc}$  that is displayed in Table 1.



The largest exit aperture of 14 mm diameter has been used in view of the fast rates of H<sub>2</sub>O(g) uptake on ice. Typical doses of H<sub>2</sub>O(g) were in the range  $10^{15}$ – $10^{17}$  ( $\pm 4 \times 10^{14}$  molecule per pulse) or between 0.05 and 5 monolayers of H<sub>2</sub>O-ice based on the geometric surface area  $S$  of the ice sample. The upper limiting temperature of the ice was 205 K beyond which evaporation led to a H<sub>2</sub>O(g) partial pressure whose mean free path violated the Knudsen flow condition and which reduced the value of  $k_{esc}$  in comparison with the value measured under molecular flow conditions. Nevertheless,  $k_c$  was obtained in the  $T$  range 205–210 K using the measured values of  $k_{esc}$ .

We have directly measured the rate  $k_c$  together with the steady-state flow rate  $F_{ss}$  of H<sub>2</sub>O(g) escaping the reactor in order to evaluate the evaporation rate  $R_{ev} = F_{ev}/V$  and flux  $J_{ev} = R_{ev} \cdot (S/V)^{-1}$ , where  $V$  is the volume of the reactor. A typical experiment is displayed in Figure 1 where the H<sub>2</sub>O(g) reference pulse is fired into the reactor with the sample compartment closed (Figure 1a, plunger lowered), whereas the reactive pulse is admitted into the flow reactor with the sample compartment open (Figure 1b, plunger lifted). At steady-state conditions and open sample compartment the rate of evaporation ( $F_{ev}$ ), condensation  $k_c[\text{H}_2\text{O}(\text{g})]V$ , and escape  $k_{esc}[\text{H}_2\text{O}(\text{g})]V$  of H<sub>2</sub>O(g) compete as expressed in the following balance of rates

$$\frac{dN}{dt} = F_{ev} - k_c N - k_{esc} N = 0 \quad [\text{molecules s}^{-1}] \quad (3)$$

where  $N$  is the total number of H<sub>2</sub>O(g) molecules present in the reactor and is given by  $[\text{H}_2\text{O}(\text{g})]V$ .

The dimensionless uptake coefficient  $\gamma$  was calculated following eq 4

$$\gamma = \frac{k_c}{\omega} \quad (4)$$

where  $\omega$  (s<sup>-1</sup>) is the collision frequency of the average H<sub>2</sub>O(g) molecule with the geometric sample surface  $S$  at 300 K and is displayed in Table 1.

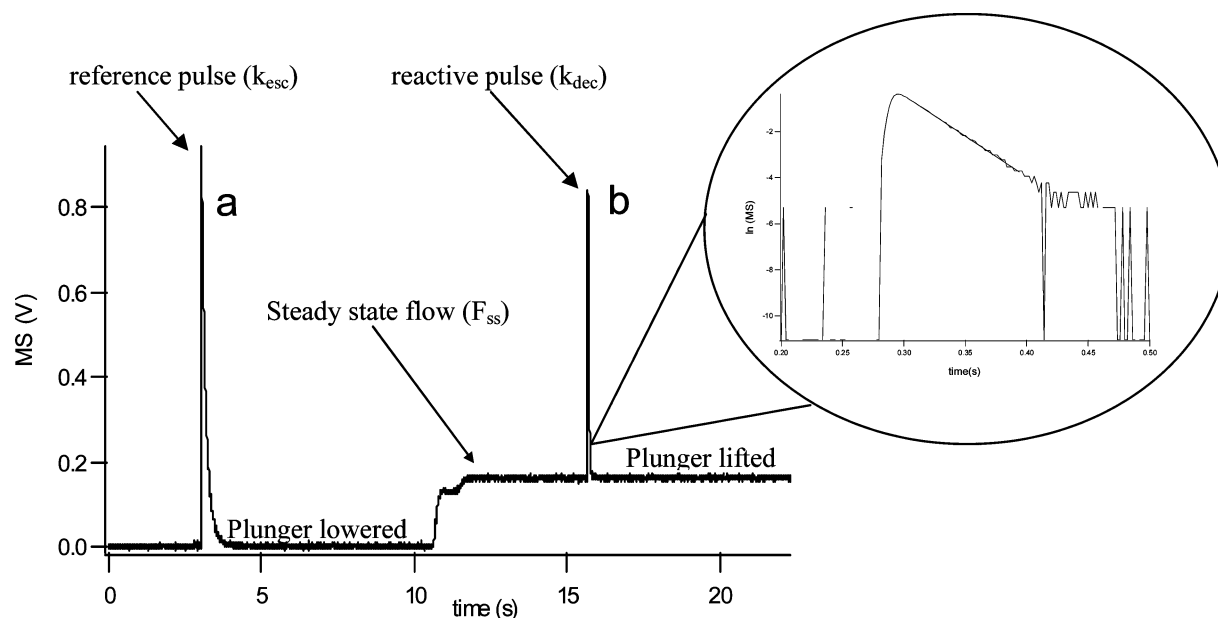


**Figure 1.** Typical pulsed valve experiment of  $\text{H}_2\text{O}(\text{g})$  interacting with bulk (B) ice at 200 K. The  $\text{H}_2\text{O}(\text{g})$  dose was  $5.0 \times 10^{16}$  molecules and corresponds approximately to 2.5 formal monolayers. Pulses a and b represent the reference and reactive pulses, respectively. The inset shows the semilogarithmic plot of the reactive decay given by  $k_{\text{dec}}$ .

Equation 3 yields after rearrangement

$$F_{\text{ev}} = F_{\text{ss}} \left( 1 + \frac{k_{\text{c}}}{k_{\text{esc}}} \right) [\text{molecules s}^{-1}] \quad (5)$$

Equation 5 puts into relation the measured steady-state  $\text{H}_2\text{O}(\text{g})$  flow rate  $F_{\text{ss}}$  at the calibrated MS signal at  $m/e$  18 as displayed in Figure 1 with the measured ratio  $k_{\text{c}}/k_{\text{esc}}$ . As discussed above,  $k_{\text{c}}$  was obtained from the exponential decay of a reactive  $\text{H}_2\text{O}(\text{g})$  pulse monitored at  $m/e$  18 as displayed in the insert of Figure 1. In the present experiments,  $k_{\text{c}}$  values of typically five separate pulsed dosing experiments at a given value of  $T$  were averaged in order to obtain an average value of  $F_{\text{ev}}$ . The temperature difference between the flow reactor (ambient  $T$ ) and the ice substrate (low  $T$ ) affects the magnitude of  $k_{\text{c}}$  such that a small correction for the thermal transpiration effect has to be applied. However, the correction of the ratio  $k_{\text{c}}/k_{\text{esc}}$  in eq 5 cancels out<sup>34</sup> and the resulting  $F_{\text{ev}}$  only depends on the temperature of the ice substrate. In addition, we have validated the transient supersaturation PV experiment by additional steady-state experiments which gave identical results. Further details may be found in Appendix A.

**2.1. MS Signal Calibration Procedure for  $\text{H}_2\text{O}$  Vapor.** The calibration of the MS signal of  $\text{H}_2\text{O}(\text{g})$  at  $m/e$  18 has been performed by freezing a water droplet of  $(9.00 \pm 0.05)$  mg mass (Mettler Toledo, AE 240 balance) deposited on the cryogenic support device described elsewhere<sup>33</sup> using a calibrated syringe. The mass of the water droplet was determined gravimetrically, and the temperature of the supported droplet rapidly decreased to 160 K. Gradually, the temperature of the droplet was increased while the  $\text{H}_2\text{O}(\text{g})$  flow rate was monitored at  $m/e$  18 as a function of time. The MS signal returned to the baseline after complete evaporation of the deposited drop after typically 30 min and at 230 K. The resulting area under the MS signal was proportional to the total number of molecules in the droplet and led to the desired calibration factor whose average is associated with a standard deviation of 5%. A blank without depositing a water droplet on the gold-plated cryogenic support resulted in deposition of 0.1% of the mass of the deposited water droplet,  $\text{H}_2\text{O}(\text{l})$ .

**2.2 Correction for Molecular Diffusion.** Pulsed valve experiments tend to underestimate the value of  $k_{\text{c}}$  at large values compared to steady-state experiments.<sup>35</sup> For a fast reaction measured in real time, a systematic bias is introduced when the  $\text{H}_2\text{O}(\text{g})$  density is depleted close to the reactive ice sample on a time scale shorter than the characteristic transit time at molecular flow conditions. To correct  $k_{\text{c}}$  for the diffusion limitation, we interpolated the curve of Fenter et al.<sup>35</sup> that correlates the measured value of  $k_{\text{c}}$  from PV experiments with  $k_{\text{c}}$  obtained from the true value of  $\gamma$  at steady state. This correction is important for measured  $k_{\text{c}}$  values larger than  $20 \text{ s}^{-1}$  which led to a correction of  $<5\%$ . The correction to  $k_{\text{c}}$  that was obtained using the PV becomes increasingly important when  $k_{\text{c}}$  tends toward  $\omega$  (Table 1).

**2.3. Preparation of Ice Samples.** The samples have been prepared in situ in the range 130–210 K using the cryogenic support whose temperature was regulated by a series 900 EUROTHERM temperature controller. Five different types of ice samples have been investigated in order to measure the kinetics of  $\text{H}_2\text{O}(\text{g})$  condensation as a function of temperature for different doses of  $\text{H}_2\text{O}(\text{g})$ . Each ice sample was prepared by using degassed bidistilled water (18.2 M $\Omega$ ).

Bulk ice (B) was prepared by pouring 5 mL of degassed bidistilled water into the cryogenic support and lowering the support temperature at a rate of  $0.2 \text{ K s}^{-1}$ . At 240 K the ice was held at this temperature for 20 min in order to avoid the buildup of stress in the sample. Subsequently, the ice was cooled to a temperature in the range between 160 and 210 K at a rate of  $0.2 \text{ K s}^{-1}$ . As displayed in Figure 2a, a typical B ice sample appears white due to its rough surface and light scattering.

Condensed (C) ice is prepared from the condensation of gas-phase  $\text{H}_2\text{O}(\text{g})$  onto the cryogenic support held at 180 K in order to form hexagonal ice.<sup>36</sup> Many parameters may be varied in the preparation of C ice, among which the  $\text{H}_2\text{O}(\text{g})$  flow rate, the residence time of  $\text{H}_2\text{O}(\text{g})$ , and the temperature of deposition. In the present experiments, we have varied the flow rate and the residence time in order to change the water concentration,  $[\text{H}_2\text{O}(\text{g})]$ , in the reactor. Three concentrations were used to form C ice, leading to  $\text{C}_1$ ,  $\text{C}_2$ , and  $\text{C}_3$  ice. As an example taken from

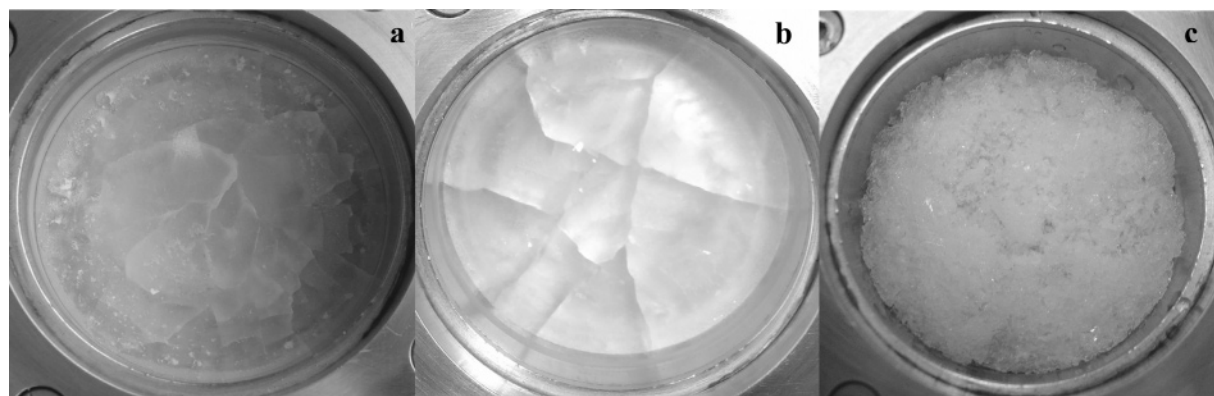


**Figure 2.** Samples of B ice (a), SC ice (b), and S ice (c) prepared in the 4.74 cm diameter cryogenic sample support. The photograph was taken at ambient temperature.

**TABLE 2: H<sub>2</sub>O Vapor Deposition Parameters for Condensed (C) Ice Samples**

type of ice	deposition time (min)	deposition temp (K)	thickness ( $\mu\text{m}$ )	[H <sub>2</sub> O] (molecules $\text{cm}^{-3}$ )	escape aperture diameter (mm)	condensation flow $F_{\text{in}} - F_{\text{out}}$ ( $\pm 5 \times 10^{13}$ molecules $\text{s}^{-1}$ )	initial flow rate $F_{\text{n}}$ ( $\pm 5 \times 10^{13}$ molecules $\text{s}^{-1}$ )
C <sub>1</sub>	50	180	2	$(7.1 \pm 0.5) \times 10^{12}$	8	$3 \times 10^{16}$	$4.1 \times 10^{16}$
C <sub>2</sub>	10	180	4	$(7.1 \pm 0.5) \times 10^{13}$	8	$3 \times 10^{17}$	$3.9 \times 10^{17}$
C <sub>3</sub>	10	180	5	$(4.4 \pm 0.9) \times 10^{15}$	1	$4 \times 10^{17}$	$4.0 \times 10^{17}$
K (cubic)	10	130	5	$(4.4 \pm 0.9) \times 10^{15}$	1	$4 \times 10^{17}$	$4.2 \times 10^{17}$

Table 2 we have used the 8 mm aperture and an initial H<sub>2</sub>O(g) flow rate of  $3.9 \times 10^{17}$  molecules  $\text{s}^{-1}$ , leading to  $[\text{H}_2\text{O}(\text{g})] = (7.1 \pm 0.5) \times 10^{13}$  molecule  $\text{cm}^{-3}$ . In this case, 75% of the initial H<sub>2</sub>O(g) flow rate  $F_{\text{in}}$  is lost from the gas phase to form C<sub>2</sub> ice at 180 K. The deposition was performed for 10 min in order to form a 4  $\mu\text{m}$  thick ice film of C<sub>2</sub> ice ( $0.75 \times 3.9 \times 10^{17}$  molecules  $\text{s}^{-1} \times 600 \text{ s}$ )/( $1.0 \times 10^{15}$  molecules  $\text{cm}^{-2} \times 17.65 \text{ cm}^2$ ). The parameters used to form C ice type are summarized in Table 2.

The deposition parameters used to generate cubic (K) ice are the same as for C<sub>3</sub> ice except for the temperature (Table 2). In this case, the temperature of the cryogenic support is lowered to 130 K and ice is formed by introducing H<sub>2</sub>O(g) into the reactor for 10 min at a flow rate indicated in Table 2. The uptake kinetics of H<sub>2</sub>O(g) is measured at 130 K using the PV technique. Subsequently, the sample previously generated at 130 K was annealed to 150 K for 10 min and cooled back to 130 K for additional uptake measurements. The same procedure was repeated for different annealing temperatures using the same K ice sample, to check for structural changes and their effects on  $k_{\text{c}}$ . Fresh K ice presumably consists of a mixture of cubic and hexagonal ice under our experimental conditions.<sup>36</sup>

Single crystal (SC) ice has been obtained by slowly freezing 5 mL of liquid degassed bidistilled water at a rate of  $1/3 \text{ K min}^{-1}$  down to 240 K in order to avoid build up of stress during crystal growth.<sup>37</sup> Subsequently, the ice was cooled to the desired temperature at a rate of  $0.2 \text{ K s}^{-1}$ . We assume that SC ice possesses a very low surface defect density in agreement with literature reports.<sup>20,36</sup> A typical SC ice sample is transparent and is displayed in Figure 2b. Visual observation of parts a and b of Figure 2 suggests that the surface roughness of B and SC ice is different. Therefore, a quantitative test was performed in order to characterize the surface roughness using the reflection of a He–Ne laser beam (UNIPHASE, 10 mW) oriented at  $10^\circ$  with respect to the surface normal of the cryogenic support. The signals  $S_{\text{B}}$ ,  $S_{\text{SC}}$ , and  $S_{\text{ref}}$  were measured for B, SC ice, and for the bare Au-plated support surface, respectively. The result

$1 - S_{\text{B}}/S_{\text{ref}} = 64 \pm 18\%$  and  $1 - S_{\text{SC}}/S_{\text{ref}} = 13 \pm 1\%$  is a measure of the scattering efficiency of the ice sample and supports the surface roughness of B ice in comparison to SC ice.

The snow (S) ice sample preparation consisted of preparing ex situ ice samples in humidified N<sub>2</sub> (relative humidity (RH) = 90% at 296 K) at atmospheric pressure and a flow of  $1 \text{ L min}^{-1}$ . To cover the entire surface of the sample holder ( $17.65 \text{ cm}^2$ ) with approximately 2 mm of loosely packed snow, a deposition of at least 1 h was required. A typical S ice sample is displayed in Figure 2c.

In the following, the units kcal/mol and Torr have been used. One multiplies the energies (kcal/mol) and the pressure (Torr) by 4.184 and 133.33, respectively, to obtain the SI units kJ/mol and Pa.

### 3. Results and Discussion

**3.1. Rate Law for the Condensation of H<sub>2</sub>O on Ice.** To determine whether the rate of H<sub>2</sub>O(g) condensation on B ice is first order in  $[\text{H}_2\text{O}(\text{g})]$ , the dependence of  $k_{\text{c}}$  or  $\gamma$  on the H<sub>2</sub>O(g) dose must be measured. Figure ESI-1 displays the uptake coefficient  $\gamma$  of H<sub>2</sub>O(g) interacting with B ice as a function of dose at different temperatures. We conclude that the kinetics of H<sub>2</sub>O(g) condensation on B ice is independent of  $[\text{H}_2\text{O}(\text{g})]$  and thus confirm the first-order kinetics of H<sub>2</sub>O(g) condensation on B ice over the dose range  $10^{15}$  to  $3.0 \times 10^{17}$  molecules.

Similar experiments were performed to test the rate law for H<sub>2</sub>O(g) uptake for C, SC, S, and K ice. Figure 3 displays data on  $\gamma(T)$  measured on C<sub>2</sub> ice for small ( $5.0 \times 10^{15}$  molecules/pulse) and large doses ( $2.0 \times 10^{17}$  molecules/pulse) as a function of  $T$  with B ice plotted as a reference. We conclude that there is no significant difference between large and small dose data which confirms that uptake of H<sub>2</sub>O(g) on C<sub>2</sub> ice follows a first-order rate law as was the case for B ice.

By changing the sample preparation conditions, the surface structure of B and C ice may change and may possibly lead to changes in  $\gamma(T)$ . If the rate at which B ice is frozen is lowered, a low defect density ice (SC) is formed which may have different kinetic properties compared to B ice.<sup>36</sup> Figure 4 shows that  $\gamma$

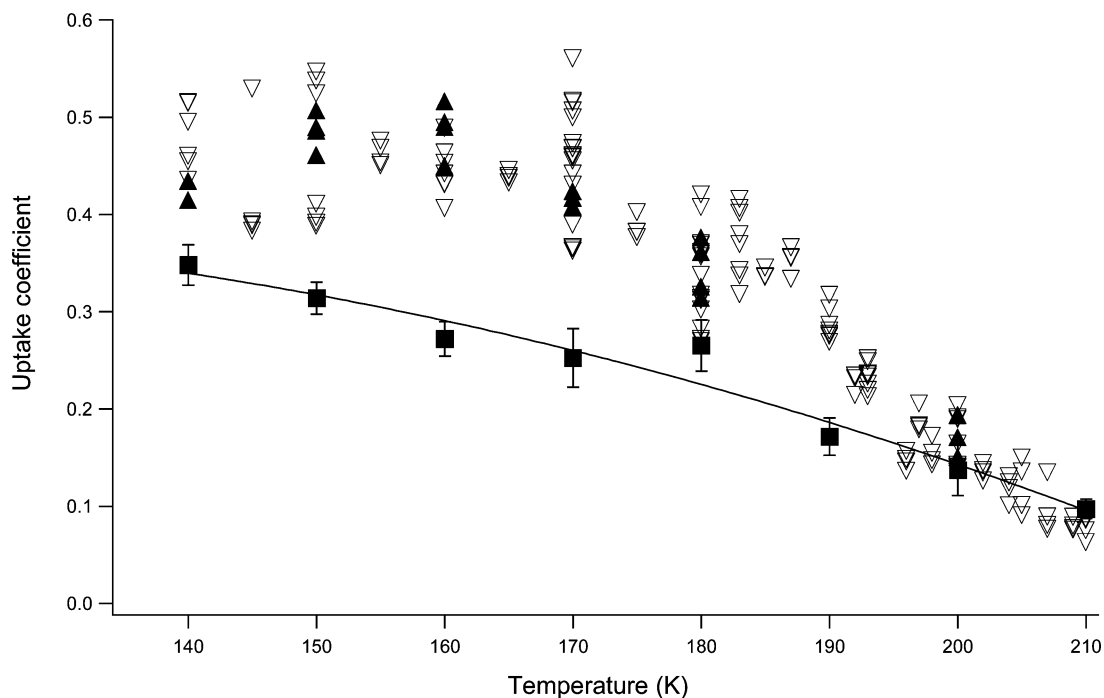


**Figure 3.** Uptake coefficient  $\gamma$  for  $C_2$  ice displayed for two different doses resulting from PV experiments: the filled ( $\blacktriangle$ ) and empty ( $\nabla$ ) triangle data correspond to doses of  $5.0 \times 10^{15}$  and  $5.0 \times 10^{16}$  molecules/pulse, respectively.  $\gamma$  for B ( $\blacksquare$ ) ice is plotted as a reference.

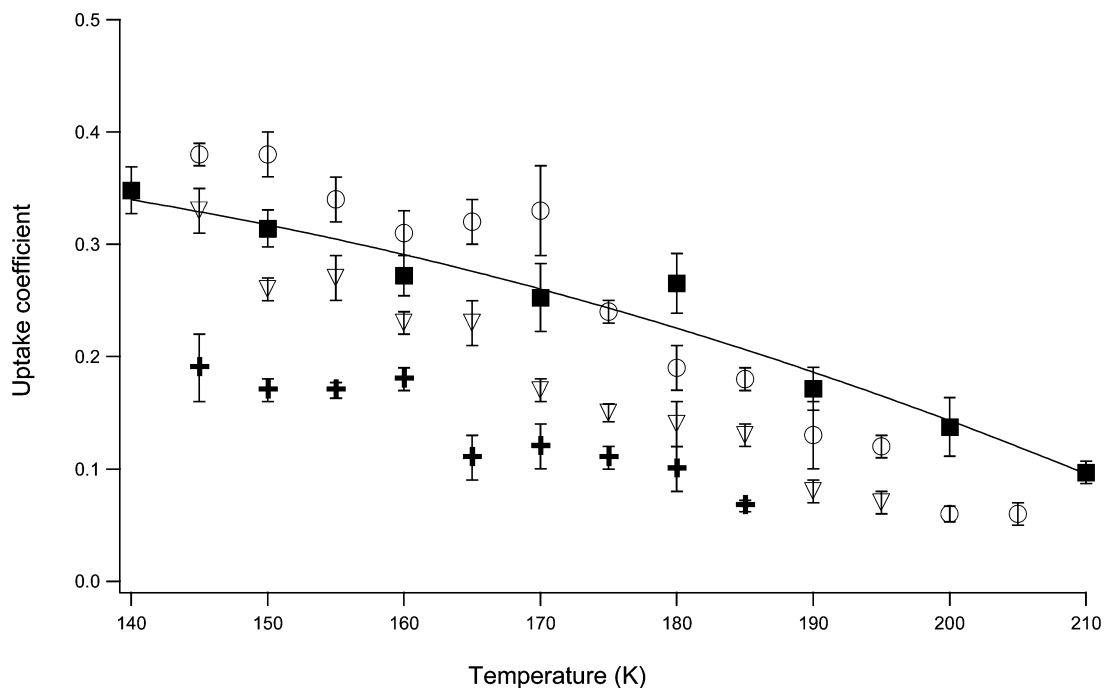


**Figure 4.** Uptake coefficient  $\gamma$  for SC ice plotted as a function of temperature for three different doses, namely,  $1.0 \times 10^{15}$  (+),  $9.0 \times 10^{15}$  ( $\nabla$ ), and  $5.0 \times 10^{16}$  (○) molecules/pulse. B ice ( $\blacksquare$ ) data are presented as a reference.

on SC ice is a function of  $T$  and of the dose when using three significantly different doses. In fact, there is a factor of 2 difference in  $\gamma$  between large ( $5.0 \times 10^{16}$  molecules/pulse) and small doses ( $1.0 \times 10^{15}$  molecules/pulse) for  $H_2O(g)$  uptake on SC ice. SC ice is a case where the kinetics of  $H_2O(g)$  condensation does not seem to follow a first-order rate law. The present work shows that  $\gamma(T)$  is larger by up to a factor of 2 when the dose or instantaneous concentration increases by a factor of 50 in the range 140–210 K.

K ice is formed like  $C_3$  ice except for the temperature of deposition (Table 2). Using three different doses differing by a factor of 50, we have observed that  $\gamma$  is independent of dose at

130 K as displayed in Figure 5. We conclude that  $H_2O(g)$  adsorption for cubic ice follows a first-order rate law.

S ice was made by slow growth of ice crystals under 1 atm of  $N_2$ . The kinetics was measured over the temperature range 136–200 K using three doses varying by a factor of 30. The results are displayed in Figure 6 which shows that there is no significant difference in  $\gamma$  for large ( $8.0 \times 10^{16}$  molecules/pulse) and small doses ( $3.0 \times 10^{15}$  molecules/pulse). In fact, the difference between the mean of the large and small dose is about 20%, which corresponds to the uncertainty of the data. Consequently, we conclude that the uptake of  $H_2O(g)$  on S ice is first order in  $H_2O$ .

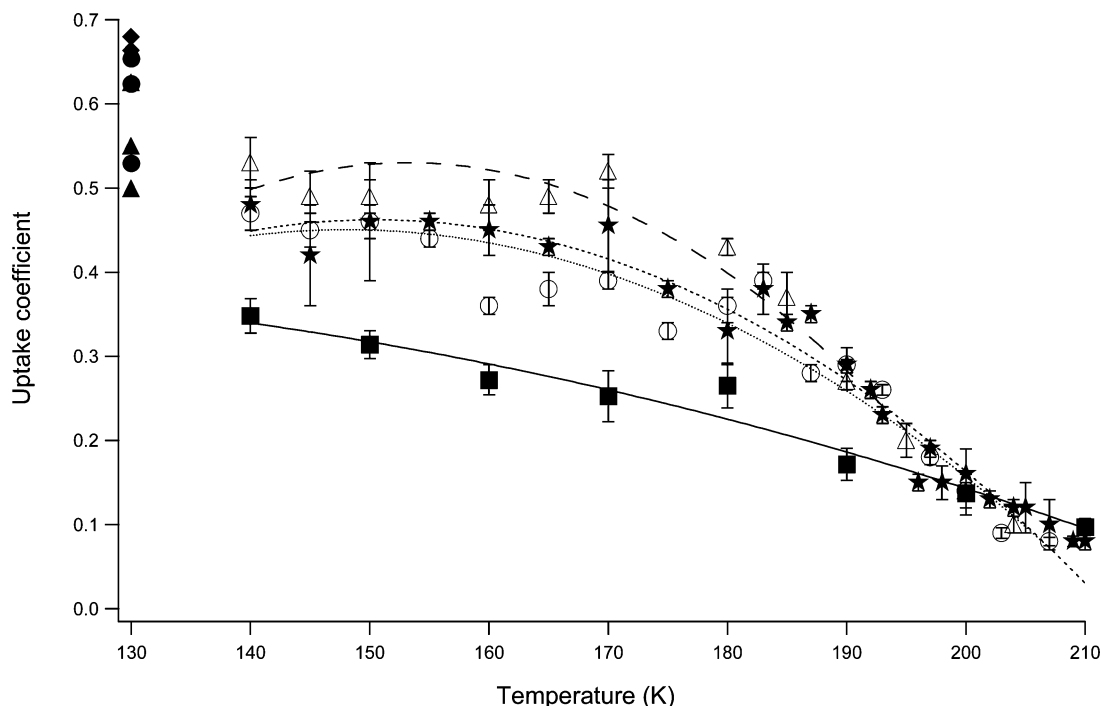


**Figure 5.** Uptake coefficient  $\gamma$  plotted as a function of temperature for three different C ice samples, namely, C<sub>1</sub> (○), C<sub>2</sub> (★), and C<sub>3</sub> (△) and using a H<sub>2</sub>O(g) dose of  $5 \times 10^{16}$  molecules/pulse. The C<sub>x</sub> deposition parameters are described in Table 2;  $\gamma$  values for B (■) and K ice are displayed as a reference. Three different doses were used to measure  $\gamma$  of K ice:  $1.5 \times 10^{15}$  (●),  $9.0 \times 10^{15}$  (◆), and  $8.0 \times 10^{16}$  (▲) molecules/pulse. The doses used on B are comprised in the range  $10^{15}$  to  $3 \times 10^{17}$  molecules and the measured kinetic of condensation was averaged over doses (Figure ESI-1).

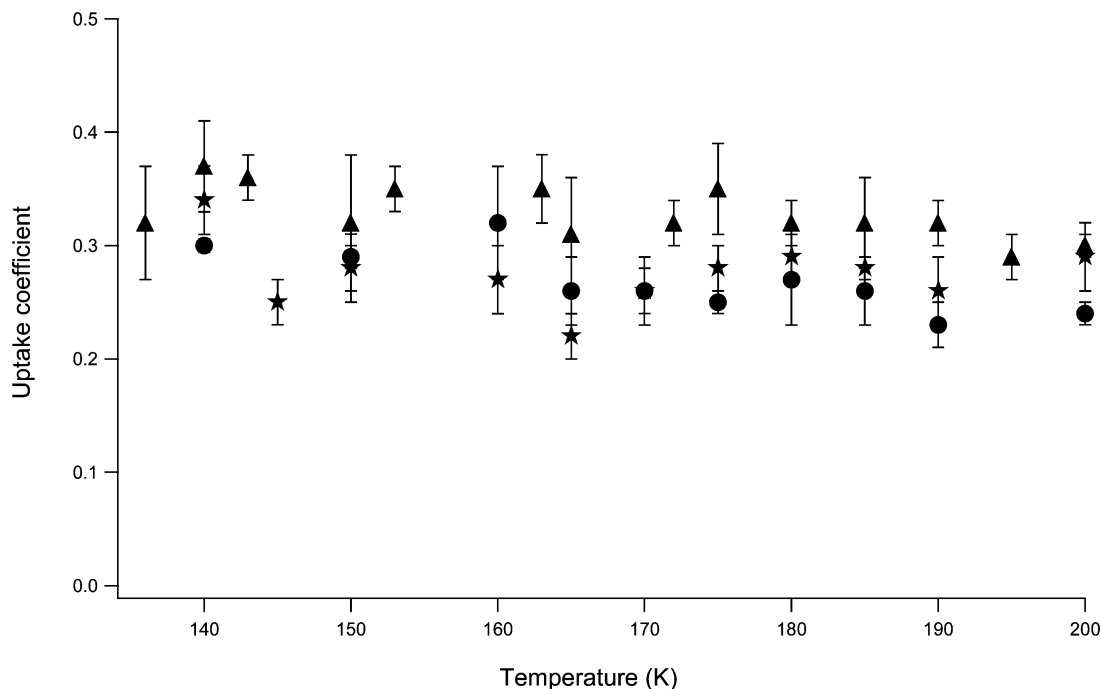


**Figure 6.** Uptake coefficient  $\gamma$  of S ice as a function of  $T$ . The different symbols compared  $\gamma$  values obtained at different doses of H<sub>2</sub>O(g):  $3.0 \times 10^{15}$  (★),  $9.0 \times 10^{15}$  (●), and  $8.0 \times 10^{16}$  (▲) molecules/pulse.

In summary, the uptake of H<sub>2</sub>O(g) on C, B, K, and S is first order in H<sub>2</sub>O while  $\gamma$  for SC seems to depend on the dose over a range of a factor of 30–50. Depending on the ice deposition/formation protocol, one must determine the rate law of H<sub>2</sub>O(g) uptake on ice if one wants to extrapolate to low supersaturations occurring in the atmosphere. Except for SC ice the use of  $\gamma$  is justified as a transferable parameter of ice growth over a temperature range characteristic of the UT/LS.

**3.2. The Dependence of  $\gamma$  on Temperature and H<sub>2</sub>O Deposition Rate for C Ice.** Typically, the limiting values of  $\gamma$

for uptake of H<sub>2</sub>O(g) on C<sub>2</sub> ice lie between  $0.48 \pm 0.04$  and  $0.08 \pm 0.03$  at 140 and 210 K (Table 3), respectively, and are plotted as a function of  $T$  in Figure 5. The data clearly show that  $\gamma$  for C<sub>2</sub> ice has a negative temperature dependence which is in agreement with a complex mechanism that implies one or more precursor species as has been found before.<sup>38,39</sup> This result is also in agreement with Haynes et al.<sup>40</sup> who confirm the negative temperature dependence first found by Davy and Somorjai<sup>1</sup> in the range 183–233 K together with the fact that  $\gamma < 1.0$  at  $T > 130$  K. However, the same workers<sup>40</sup>

**TABLE 3: Range of  $\gamma$  for Different Types of Ice**

type of ice <sup>a</sup>	$\gamma$	temp (K)
B	0.35 $\pm$ 0.02 to 0.10 $\pm$ 0.02	140–210
C <sub>2</sub>	0.48 $\pm$ 0.04 to 0.08 $\pm$ 0.03	140–210
SC (L)	0.38 $\pm$ 0.01 to 0.06 $\pm$ 0.01	145–205
SC (M)	0.33 $\pm$ 0.02 to 0.08 $\pm$ 0.01	145–195
SC (S)	0.20 $\pm$ 0.03 to 0.10 $\pm$ 0.02	145–185
S	0.32 $\pm$ 0.05 to 0.29 $\pm$ 0.02	136–200
K	0.64 $\pm$ 0.05	130

<sup>a</sup> L, M, and S are large, medium, and small doses corresponding to  $5.0 \times 10^{16}$ ,  $9.0 \times 10^{15}$ , and  $1.0 \times 10^{15}$  molecules/pulse.

unfortunately revoked their results later by setting  $\gamma = 1.0$  across the entire temperature range of 20–185 K in order to determine the optical constants for the used ice films.<sup>41</sup>

The way C ice is formed may potentially change the kinetic properties of the ice surface. For that reason  $k_c$  was measured for three different [H<sub>2</sub>O(g)] (C<sub>1</sub>, C<sub>2</sub>, C<sub>3</sub>) differing by a factor of 600 and displayed in Table 2. The kinetic results are displayed in Figure 5 where  $\gamma$  is plotted as a function of temperature for C<sub>1</sub>, C<sub>2</sub>, and C<sub>3</sub> ices. The results show that  $\gamma$  for C ice increases somewhat with the H<sub>2</sub>O(g) concentration varied by a factor of 600. Taking the two extreme cases C<sub>3</sub> vs C<sub>1</sub> ice, the former presents a  $\gamma$  value approximately 10–30% larger for  $T < 190$  K compared to C<sub>1</sub>. However, we do not find a significant dependence of  $\gamma$  on the H<sub>2</sub>O(g) deposition rate for C ice at  $T > 190$  K as all values seem to merge to a common value as displayed in Figure 5. This may be an indication that the mechanism of H<sub>2</sub>O(g) uptake may change around 190 K, as will be discussed below.

Haynes et al.<sup>40</sup> have performed measurements of  $\gamma$  by isothermal evaporation of C ice in the range 20–185 K. They obtained  $\gamma = 0.75$  and 0.69 at 160 and 185 K, respectively, in contrast to the present values for C<sub>1</sub> ice which lie between  $\gamma = 0.36 \pm 0.04$  at 160 K and  $\gamma = 0.32 \pm 0.06$  at 185 K. It is likely that the vapor deposition conditions used by Haynes et al.<sup>40</sup> were closer to C<sub>1</sub> than to C<sub>3</sub> deposition conditions (Table 2). This discrepancy of approximately a factor of 2 in  $\gamma$  may perhaps be explained by the fact that  $\gamma$  depends on the way the ice sample was prepared. In fact, they measured  $\gamma$  between 20 and 185 K on ice condensed from H<sub>2</sub>O(g) at a total pressure ranging from  $3.3 \times 10^{-6}$  to  $6.6 \times 10^{-5}$  Torr. In contrast, in this work C<sub>1</sub> ice was deposited at 180 K at a pressure of  $2.20 \pm 0.15 \times 10^{-4}$  Torr which is higher by at least a factor of 3. This and the different temperature of deposition may lead to structural differences and therefore to changes of reactivity toward H<sub>2</sub>O(g) vapor. Delval and Rossi<sup>42</sup> measured a  $\gamma$  value of 0.38 and 0.12 at 185 and 207 K, respectively, on C ice condensed at 190 K at a H<sub>2</sub>O(g) flux of  $1.0 \times 10^{17}$  molecules s<sup>-1</sup> cm<sup>-2</sup> compared to  $1.7 \times 10^{15}$  molecules s<sup>-1</sup> cm<sup>-2</sup> of H<sub>2</sub>O(g) in the present study. Within the uncertainty of the present measurement, namely,  $\gamma = 0.32 \pm 0.06$  and  $0.08 \pm 0.05$  at 185 and 207 K, respectively,  $\gamma$  for C<sub>1</sub> ice is in agreement with Delval et al.<sup>42</sup> Moreover, the agreement improves for C<sub>3</sub> ice resulting in  $\gamma = 0.37 \pm 0.06$  and  $0.10 \pm 0.04$  at 185 and 207 K, respectively, at a deposition flux of  $2.3 \times 10^{16}$  molecules s<sup>-1</sup> cm<sup>-2</sup>, which approaches the H<sub>2</sub>O(g) flux used by Delval et al.<sup>42</sup>

**3.3. The Evaporation Flux ( $J_{ev}$ ) from C Ice.** The evaporation rate,  $F_{ev}$ , in molecules s<sup>-1</sup>, was obtained from eq 5 by measuring  $k_c$  and  $F_{ss}$  in the same experiment as displayed in Figure 1. As an example, the evaporative flux,  $J_{ev}$  in molecules cm<sup>-2</sup> s<sup>-1</sup>, is displayed in Figure 7 and Table ESI-1. The solid line corresponds to the maximum theoretical value,  $J_{ev}^{max}$ , that is obtained by setting  $\gamma$  to unity using the vapor pressure  $P_{eq}$  of

Marti and Mauersberger<sup>43</sup> that has been extrapolated for  $T < 165$  K. Delval and Rossi have recently measured  $J_{ev}$  using a microbalance technique in a stirred flow reactor at temperatures ranging from 172 to 203 K.<sup>42</sup> Their results match the present  $J_{ev}$  data for C<sub>2</sub> ice in this interval within 25%. Moreover, they have measured  $J_{ev}$  at  $T > 196$  K using a stirred flow reactor technique<sup>34</sup> that agrees with the present data to within 10%. The results of Smith et al.<sup>44</sup> and Haynes et al.<sup>40</sup> are in very good agreement with the present values of  $J_{ev}$  for C<sub>2</sub> ice and with the microbalance data of Delval and Rossi<sup>42</sup> to within 35% which is remarkable in view of the different experimental techniques invoked.  $J_{ev}$  measured at 170 K by Fraser et al.<sup>45</sup> is a factor of 2 larger than the present data for C<sub>2</sub> ice. More serious is the discrepancy in  $J_{ev}$  between the data of Davy and Somorjai<sup>1</sup> and the present values: the former measure  $J_{ev}$  values that are larger by roughly a factor of 10 in the range 186–218 K. In contrast,  $J_{ev}$  measured by Sack and Baragiola<sup>46</sup> significantly exceeds the maximum evaporation flux  $J_{ev}^{max}$  in the range 135–170 K. At 150 and 170 K,  $J_{ev}$  exceeds  $J_{ev}^{max}$  by 250% and 30%, respectively, for no apparent reason. In summary, although  $J_{ev}$  of C ice depends somewhat on the used H<sub>2</sub>O(g) deposition rate for the generation of C ice as measured from the corresponding  $\gamma$  values (Figure 5), all  $J_{ev}$  values are significantly smaller than  $J_{ev}^{max}$  and imply a  $\gamma$  value significantly lower than unity between 140 and 240 K. The discrepancy between  $J_{ev}^{max}$  and  $J_{ev}$  thereby increases with  $T$ .

**3.4. The Dependence of  $\gamma$  on Temperature for Other Types of Ice.** The  $\gamma$  value for B ice varies between 0.35  $\pm$  0.02 and 0.10  $\pm$  0.02 in the range 140–210 K as displayed in Table 3. Like for C<sub>2</sub> ice,  $\gamma$  of H<sub>2</sub>O(g) interacting with B ice is significantly lower than unity and Figure 3 displays the measured  $\gamma$  values for B and C<sub>2</sub> ice at different temperatures. Interestingly,  $\gamma$  for S ice does not change significantly with  $T$  as displayed in Figure 6 for three different doses. Table 3 shows that  $\gamma$  lies between 0.32  $\pm$  0.05 and 0.29  $\pm$  0.02 in the range 136–200 K in agreement with Chaix et al.<sup>38</sup> who observed the same weak dependence of  $k_c$  on  $T$  in the range 140–220 K. SC ice is a special case because  $k_c$  does not follow a first-order rate law as discussed above (Figure 4). The  $\gamma$  value changes from 0.38  $\pm$  0.01 to 0.057  $\pm$  0.007 for a large dose of  $5.0 \times 10^{16}$  molecules/pulse in going from 145 to 205 K. For a small dose of  $1.0 \times 10^{15}$  molecules/pulse,  $\gamma$  changes from 0.20  $\pm$  0.03 to 0.10  $\pm$  0.02 from 145 to 185 K as displayed in Figure 4 where  $\gamma$  is plotted for three doses as a function of  $T$  spanning a factor of 50 in dose. We note from Figure 4 that  $\gamma$  for B ice seems to be higher at  $T > 180$  K and lower at  $T < 180$  K compared to SC ice for a high dose of  $5.0 \times 10^{16}$  molecules/pulse probing the surface. In contrast,  $\gamma$  measured on SC ice seems to be smaller compared to B ice for medium ( $9.0 \times 10^{15}$  molecules/pulse) and low doses ( $1.0 \times 10^{15}$  molecules/pulse). The particular case of K ice was studied at  $T = 130$  K where  $k_c$  is significantly larger than for the other types of ice studied so far. The cubic ice I<sub>c</sub> morphology seems to be more reactive toward condensation of H<sub>2</sub>O(g) vapor compared to the hexagonal I<sub>h</sub> ice structure and leads to an average  $\gamma$  of 0.64  $\pm$  0.05 at 130 K as displayed in Figure 5. The results for K ice confirm that the PV uptake experiment for all types of ice except for K ice is not limited by instrumental parameters. Several pulse decays are plotted in a semilogarithmic fashion as a function of time in Figure 8 in order to show different pulse decay rates for different types of ice at different temperatures. As an example, the pulse decay for fresh K ice at 130 K is larger by a factor of 4 compared to a C<sub>2</sub> ice sample at 200 K. This comparison displays the typical range of variation in  $k_c$  for different ice samples. In conclusion,

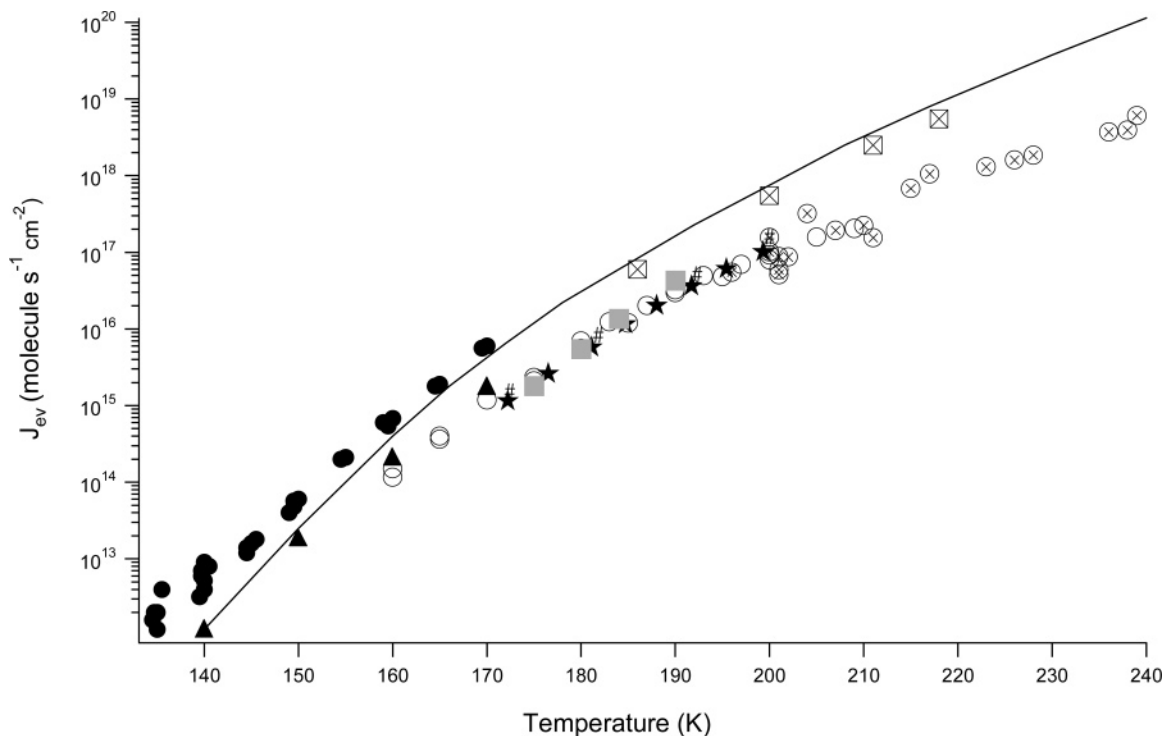


**Figure 7.** The evaporation flux  $J_{ev}$  of H<sub>2</sub>O(g) for C<sub>2</sub> ice as a function of  $T$  compared to values from the literature in the range 136–240 K: (× inside a square) Davy et al.;<sup>1</sup> (#) Haynes et al.;<sup>40</sup> (▲) Fraser et al.;<sup>45</sup> (shaded square) Smith et al.;<sup>44</sup> (●) Sack et al.;<sup>46</sup> (★) Delval and Rossi<sup>42</sup> (microbalance experiment); (× inside a circle) Delval et al.<sup>34</sup> (stirred flow reactor). This work: (○) pulsed valve experiment on C<sub>2</sub> ice at a dose of  $5.0 \times 10^{16}$  molecules/pulse.

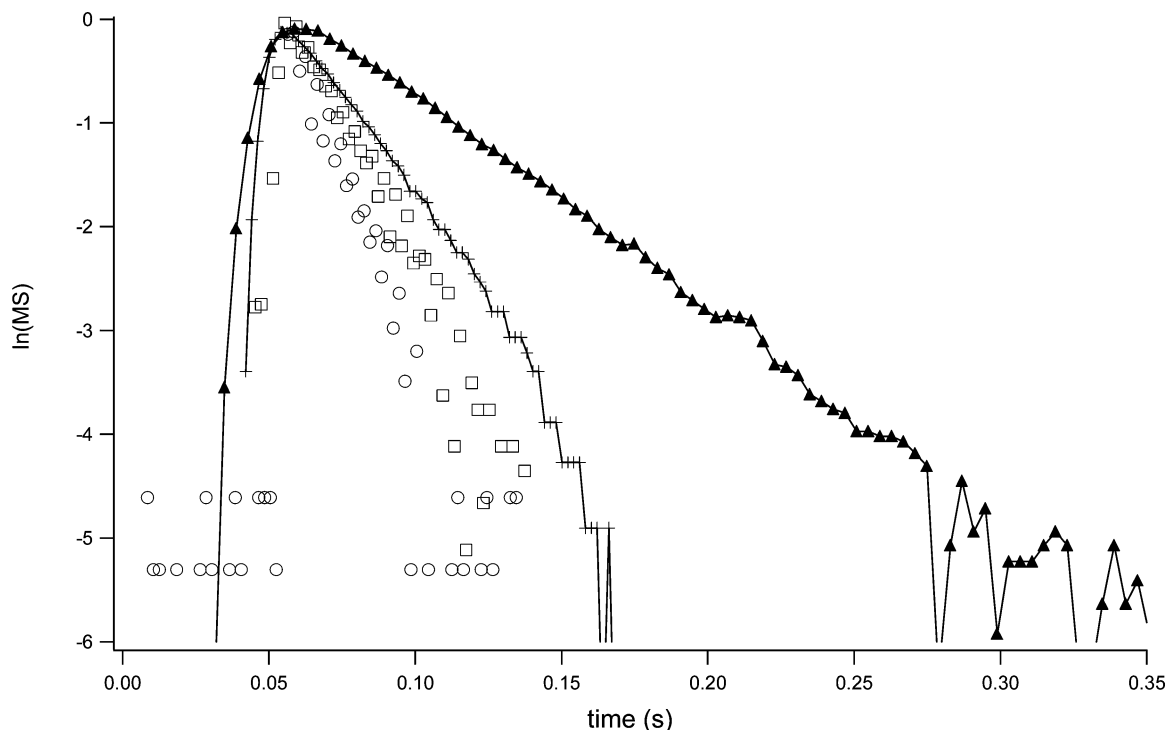


**Figure 8.** Typical decay kinetics for condensation of H<sub>2</sub>O(g) on different ice samples. A dose of  $5.0 \times 10^{16}$  molecules/pulse was used for each of the four pulses. The triangle (▲) corresponds to  $k_c = 20 \text{ s}^{-1}$  for C<sub>2</sub> ice at 207 K, the (+) symbol to  $k_c = 38 \text{ s}^{-1}$  for B ice at 200 K, and the circle (○) and the square (□) are pulse decays for fresh K ice ( $68 \text{ s}^{-1}$ ) at 130 K and for the same K ice sample annealed at 170 K and measured at 130 K ( $51 \text{ s}^{-1}$ ), respectively.

$\gamma$  is significantly different for different types of ice. For  $T < 185 \text{ K}$ , we have the following sequence:  $\gamma(\text{K}) > \gamma(\text{C}_2) > \gamma(\text{SC,L}) > \gamma(\text{B}) \approx \gamma(\text{S})$ . For  $T > 185 \text{ K}$ ,  $\gamma(\text{S}) > \gamma(\text{C}_2) \approx \gamma(\text{B}) > \gamma(\text{SC,L})$ , where L means a large dose of typically  $5 \times 10^{16}$ , compared to a small dose of  $1.0 \times 10^{15}$  molecules/pulse.

### 3.5. The Evaporation Flux ( $J_{ev}$ ) for Other Types of Ice.

In addition to  $J_{ev}$  for C<sub>2</sub> discussed above, we have determined  $J_{ev}$  on the other types of ice, namely, for B, SC, and S ice that are displayed in Figure 9 and Tables ESI-2, ESI-3, ESI-4 and ESI-5 as a function of  $T$ . Except for K ice, we conclude that C<sub>2</sub>



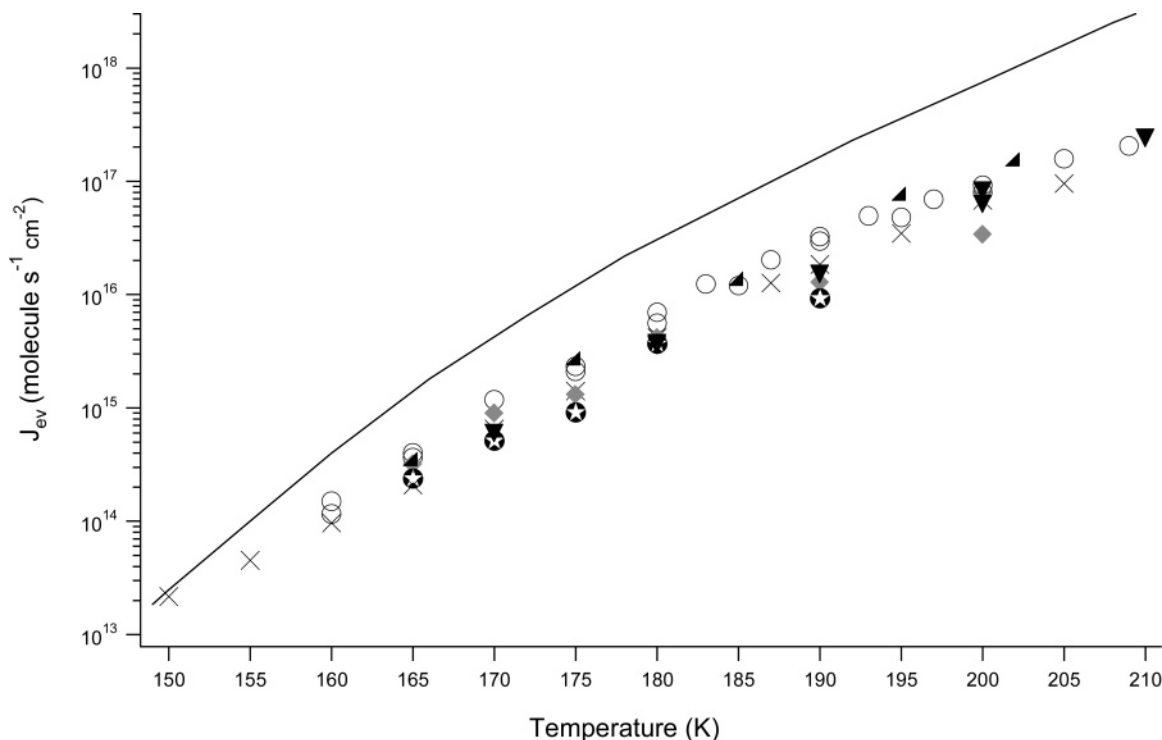


**Figure 9.**  $J_{\text{ev}}$  of  $\text{H}_2\text{O}(\text{g})$  as a function of temperature for the different types of ice between 150 and 210 K: ( $\blacktriangledown$ ) CFM experiment (Appendix A) on B ice; ( $\times$ ) PV experiment on B ice; ( $\circ$ ) PV experiment on  $\text{C}_2$  ice; (shaded diamond) PV experiment on SC (large dose,  $5.0 \times 10^{16}$  molecules/pulse); (star in solid circle) PV experiment on SC (medium dose,  $9.0 \times 10^{15}$  molecule/pulse); (solid right triangle) S ice. The dose for B,  $\text{C}_2$ , and S ice was  $5.0 \times 10^{16}$  molecules/pulse. The full line represents  $J_{\text{ev}}^{\text{max}}$  using  $P_{\text{eq}}$  from the literature.<sup>43</sup> Values of  $P_{\text{eq}}$  below 165 K have been extrapolated.

ice has the largest value of  $J_{\text{ev}}$  and  $k_{\text{c}}$  compared to the other types of ice studied in this work. In contrast, the lowest value of  $J_{\text{ev}}$ , paired with the lowest value of  $k_{\text{c}}$  is found for SC ice using a medium dose ( $9.0 \times 10^{15}$  molecule/pulse) to probe the surface (Figures 4 and 9). In fact,  $J_{\text{ev}}$  for B ice is from 40 to 80% lower compared to  $\text{C}_2$  ice which is outside of the present measurement uncertainty.  $J_{\text{ev}}$  for SC ice at the large dose of  $5.0 \times 10^{16}$  molecules/pulse is smaller by a factor of 2 at  $T = 200$  K and approximately 10% larger at  $T = 175$  K compared to B ice. For other  $\text{H}_2\text{O}(\text{g})$  doses  $J_{\text{ev}}$  for SC ice changes as displayed in Figure 9 consistent with the dependence of  $\gamma$  on the dose shown in Figure 4.  $J_{\text{ev}}$  for S ice seems to match with the  $\text{C}_2$  ice data set to within 20–50% in the range 165–202 K according to Figure 9. In summary, we obtain the sequence  $J_{\text{ev}}(\text{C}_2) > J_{\text{ev}}(\text{B}) \approx J_{\text{ev}}(\text{S}) > J_{\text{ev}}(\text{SC})$  in the range 150–210 K. In contrast to Chaix et al.<sup>38</sup> we obtain a  $\gamma$  value for C ice that is larger compared to B ice. This difference may perhaps be attributed to the conditions of deposition such as  $\text{H}_2\text{O}(\text{g})$  flow rate and temperature. However, we conclude in agreement with Chaix et al.<sup>38</sup> that SC ice presents a lower reactivity compared to B and C ice, probably owing to a low density of surface defects. Except for Chaix et al.,<sup>38</sup> no other work has been performed on both  $J_{\text{ev}}$  and  $\gamma$  while systematically varying the type of ice such as B, SC, and S. Consequently, comparisons with other results work are difficult. In agreement with the conclusion of Chaix et al.<sup>38</sup> the present work supports the conclusion that ices that present stress cracks and grain boundaries show larger values of  $J_{\text{ev}}$  and  $k_{\text{c}}$ .<sup>20</sup> However, the equilibrium vapor pressure is independent of the type of ice as will be discussed also below.

**3.6. Annealing Studies on K Ice.** At  $T > 130$  K the cubic structure of K ice ( $\text{I}_\text{c}$ ) should progressively convert to the hexagonal ice structure  $\text{I}_\text{h}$ .<sup>38</sup> As discussed by Davy and Somorjai<sup>1</sup> and Kumai,<sup>36</sup> K ice is transformed completely to  $\text{I}_\text{h}$  ice at  $T > 173$  K after only 75 min. In the following experiment we

have measured  $\gamma$  on K ice at 130 K using a  $\text{H}_2\text{O}(\text{g})$  pulse as a surface probe at a dose ranging from  $(0.15 \text{ to } 8.0) \times 10^{16}$  molecules/pulse. Subsequently, K ice was annealed to 150 K for 10 min before it was cooled to 130 K in order to measure  $\gamma$  once more. This is displayed in Figure 10 where  $\gamma$  obtained at the sample temperature of 130 K is plotted as a function of the annealing temperature. We note that for an annealing temperature of 150 K,  $\gamma$  decreases by 10% compared to fresh K ice. We observe a further decrease of  $\gamma$  with increasing annealing temperature. For an annealing temperature of 190 K,  $\gamma$  measured at 130 K decreases by 40% compared to fresh K ice. Similar results were observed by Chaix et al.<sup>38</sup> for  $\text{D}_2\text{O}$  ice and thus confirm the present results although the latter results for both  $\gamma$  and  $J_{\text{ev}}$  were slightly larger compared to the present values. For  $T_{\text{annealing}} = 190$  K,  $\gamma$  of K ice is identical to  $\gamma$  obtained for  $\text{C}_3$  ice measured at 140 or 150 K. A blank annealing run of  $\text{C}_3$  ice deposited at 180 K and treated in an identical manner as K ice confirmed the thermodynamic stability of  $\text{I}_\text{h}$  ice under the present experimental conditions. We conclude that metastable cubic ice  $\text{I}_\text{c}$  domains are irreversibly converted into  $\text{I}_\text{h}$  ice in the annealing process which assume the kinetic properties of  $\text{C}_3$  ice after annealing. As showed in Appendix B, the negative  $T$  dependence is also observed on thermodynamically stable ice crystal phase  $\text{I}_\text{h}$ . If the  $T$  dependence is in the presence of metastable phase, we should observed a time-dependent value of  $k_{\text{c}}$ , which is not the case. Further details are discussed in Appendix B.

**3.7. Thermochemical Parameters for  $\text{C}_2$  Ice.** Figure 11 presents an Arrhenius plot of  $k_{\text{c}}$  for  $\text{C}_2$  ice which clearly displays two temperature regimes whose transition occurs at  $T_{\text{break}} = 190 \pm 3$  K and leads to a high- and low-temperature regime for  $T > 190$  K and  $T < 190$  K, respectively. The slopes of the straight lines displayed in Figure 11 lead to a negative energy of activation for condensation  $E_{\text{a}}^{\text{c}} = -4.1 \pm 1.4$  kcal/mol for  $T > 190$  and  $E_{\text{a}}^{\text{c}} = -0.18 \pm 0.14$  kcal/mol for  $T < 190$  K. A

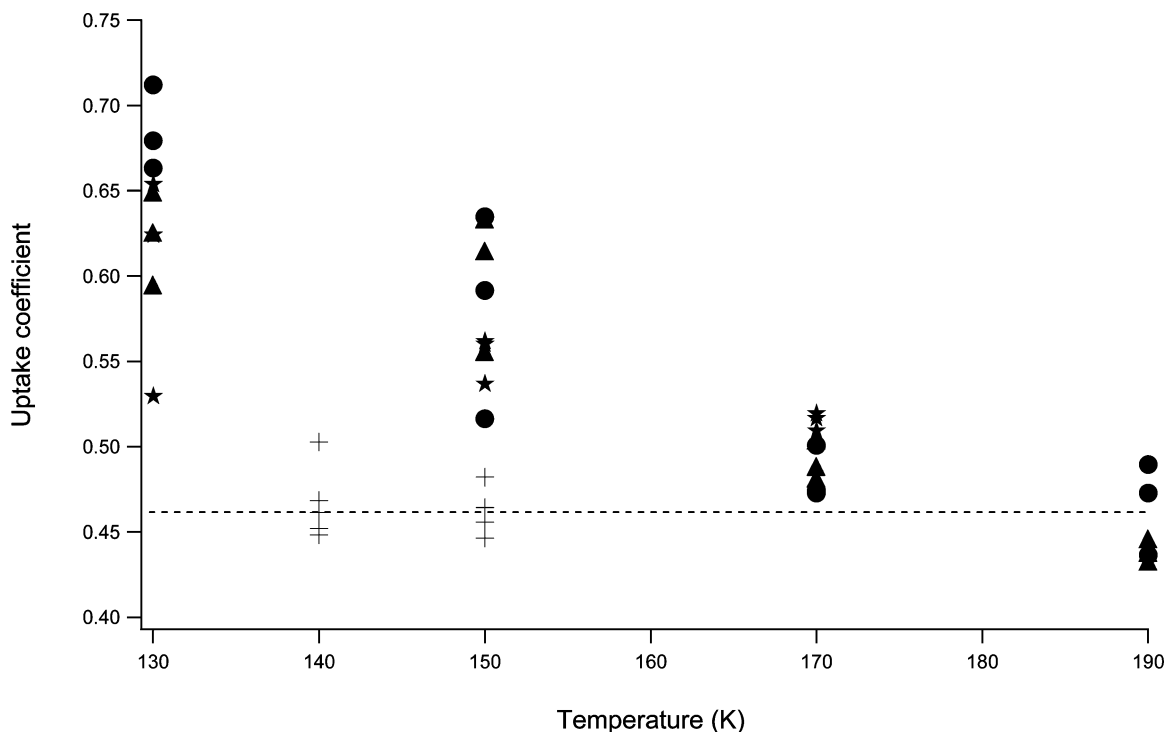


**Figure 10.**  $\gamma$  on K ice as a function of annealing temperature in comparison to  $\gamma$  of C<sub>3</sub> ice (+). Three different doses are used to probe the kinetics on K ice, namely,  $1.5 \times 10^{15}$  ( $\star$ ),  $9.0 \times 10^{15}$  ( $\bullet$ ), and  $5.0 \times 10^{16}$  ( $\blacktriangle$ ) molecules/pulse. The kinetic measurement was performed at 130 K for all substrates.

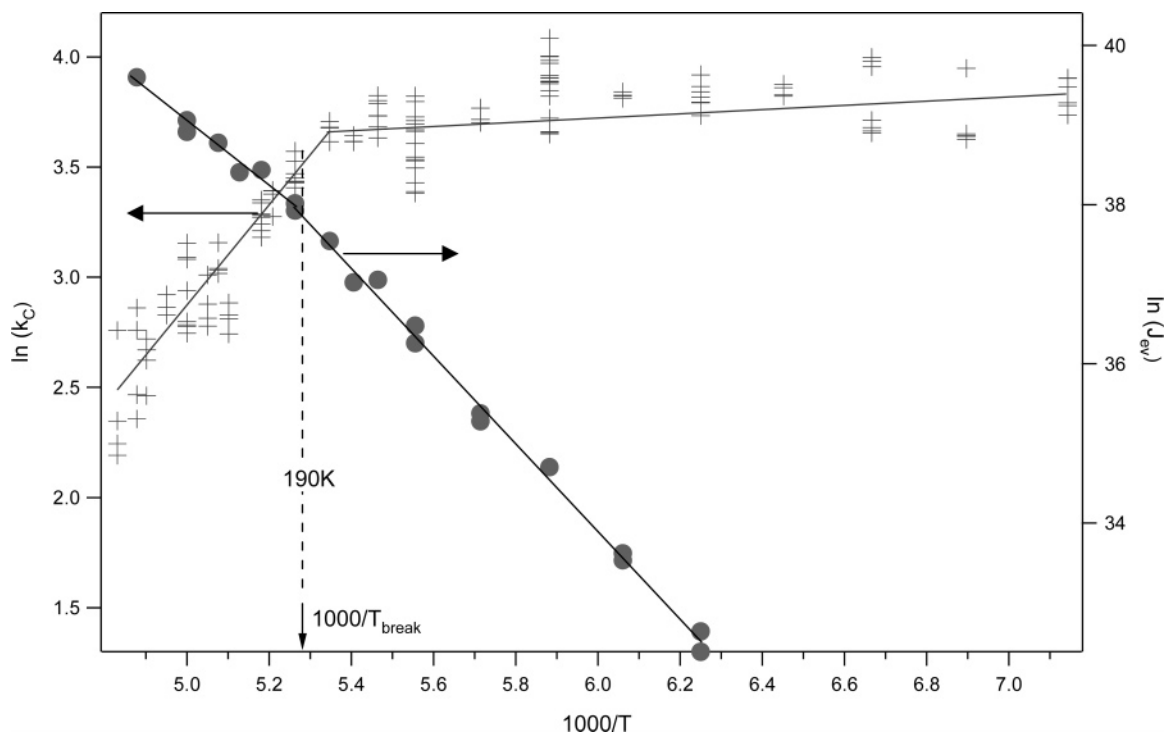


**Figure 11.** Arrhenius representation of  $k_c$  and  $J_{ev}$  for C<sub>2</sub> ice whose values are displayed in Table ESI-1 for  $J_{ev}$  and in Figure 3 for  $k_c$ . Two  $T$  regimes are apparent at the discontinuity  $T_{break} = 190$  K. The activation energy for  $k_c$  at  $T < 190$  K is  $E_a^c = -0.18 \pm 0.14$  and  $-4.1 \pm 2.1$  kcal mol<sup>-1</sup> for  $T > 190$  K and for  $J_{ev}$   $11.9 \pm 1.3$  and  $7.9 \pm 1.2$  kcal mol<sup>-1</sup>, respectively (Tables 4 and 5).

similar discontinuity in the Arrhenius plot of  $k_c$  has recently been observed for  $\gamma$  on C ice<sup>42</sup> at 193 K which is identical within experimental uncertainty to the break observed in this work. Delval and Rossi<sup>42</sup> obtained  $E_a^c = -1.5 \pm 0.5$  and  $-0.3 \pm 0.1$  kcal/mol for  $T > 190$  and  $T < 190$  K, respectively. The change in the energy of activation  $E_a^c$  for C<sub>2</sub> ice at  $T > 190$  K may be explained by a shift of the rate-limiting step with increasing  $T$  in the precursor mechanism that is discussed by Flückiger and

Rossi.<sup>39</sup> As pointed out above, the merging of  $\gamma$  values at different H<sub>2</sub>O(g) doses for C ice at  $T > 190$  K displayed in Figure 5 may have the same mechanistic origin in that the rate-limiting step in this  $T$  range is insensitive to the type of ice.

An additional way to characterize the ice surface from a kinetic point of view is to measure the energy of activation of evaporation  $E_a^{ev}$ . By plotting the  $J_{ev}$  data displayed in Figure 9 in an Arrhenius fashion, we obtain  $E_a^{ev}$  for C<sub>2</sub> ice. The  $J_{ev}$  data

**TABLE 4: Energy of Activation  $E_a^c$  for Condensation of  $H_2O(g)$** 

type of ice	$E_a^c$ (kcal/mol)						$T_{\text{break}}$ (K)
	Delval et al. <sup>42</sup>		Chaix et al. <sup>38</sup>		present work		
	193–223 K	182–193 K	190–220 K	140–190 K	$T \geq T_{\text{break}}$	$T < T_{\text{break}}$	
C <sub>2</sub>	-1.5 ± 0.5	-0.3 ± 0.1	-4.2 ± 1	-0.24 ± 0.05	-4.1 ± 1.4	-0.18 ± 0.14	190 ± 3
B			-4.2 ± 1.7	-0.26 ± 0.13	-2.3 ± 0.9	-0.24 ± 0.11	185 ± 3
SC (L <sup>a</sup> dose)					-3.1 ± 0.6	-0.26 ± 0.15	170 ± 5
SC (M <sup>a</sup> dose)						-2.8 ± 0.8	no break
S						-0.3 ± 0.2	no break

<sup>a</sup> Key: L = large dose ( $5.0 \times 10^{16}$  molecules/pulse); M = medium dose ( $9.0 \times 10^{15}$  molecules/pulse).

**TABLE 5: Energy of Activation  $E_a^{\text{ev}}$  for Evaporation of  $H_2O(g)$** 

type of ice	$E_a^c$ (kcal/mol)						$T_{\text{break}}$ (K)
	Delval et al. <sup>42</sup>		Chaix et al. <sup>38</sup>		present work		
	193–223 K	173–193 K	190–220 K	140–190 K	$T \geq T_{\text{break}}$	$T < T_{\text{break}}$	
C <sub>2</sub>	+10.2 ± 0.5	+12.0 ± 0.5			7.9 ± 1.2	11.9 ± 1.3	190 ± 3
B			+8.3 ± 1.0	+12.2 ± 0.5	9.9 ± 0.8	11.5 ± 1.0	185 ± 3
SC (L <sup>a</sup> dose)					8.5 ± 0.5	11.6 ± 0.8	170 ± 5
SC (M <sup>a</sup> dose)						9.5 ± 0.8	no break
S						11.5 ± 0.6	no break

<sup>a</sup> Key: L = large dose ( $5.0 \times 10^{16}$  molecules/pulse); M = medium dose ( $9.0 \times 10^{15}$  molecules/pulse).

**TABLE 6: Enthalpy of Sublimation  $\Delta H_S^\circ$  of  $H_2O(g)$  from Ice Obtained from Tables 4 and 5**

type of ice	$E_a^c$ (kcal/mol)						entropy (cal K <sup>-1</sup> mol <sup>-1</sup> )	$T_{\text{break}}$ (K)
	Delval et al. <sup>42</sup>		Chaix et al. <sup>38</sup>		present work			
	193–223 K	182–193 K	190–220 K	140–190 K	$T \geq T_{\text{break}}$	$T < T_{\text{break}}$		
C <sub>2</sub>	11.7 ± 0.6	12.3 ± 0.5			12.0 ± 2.6	12.1 ± 1.5	34.6 ± 2.5	190 ± 3
B			12.5 ± 2.7	12.5 ± 0.6	12.2 ± 1.7	11.8 ± 1.1	29.8 ± 1.9	185 ± 3
SC (L <sup>a</sup> dose)					11.6 ± 1.1	11.9 ± 1.0	34.1 ± 2.1	170 ± 5
SC (M <sup>a</sup> dose)						12.3 ± 1.6	33.9 ± 2.4	no break
S						11.8 ± 0.8	33.6 ± 1.8	no break

<sup>a</sup> Key: L = large dose ( $5.0 \times 10^{16}$  molecules/pulse); M = medium dose ( $9.0 \times 10^{15}$  molecules/pulse).

also show a discontinuity at  $T = 190 \pm 3$  K similar to  $k_c$  and are displayed in Figure 11 which shows that the break in  $k_c$  coincides with the one for  $J_{\text{ev}}$  at 190 K as it should. The data displayed in Figure 11 obtain  $E_a^{\text{ev}} = 7.9 \pm 1.2$  for  $T > 190$  K and  $E_a^{\text{ev}} = 11.9 \pm 1.3$  kcal/mol for  $T < 190$  K. In comparison with Delval and Rossi<sup>42</sup> who obtain  $E_a^{\text{ev}} = 10.2 \pm 0.5$  and  $12.0 \pm 0.5$  kcal/mol above and below  $193 \pm 3$  K, respectively, we note a disagreement between the present  $E_a^{\text{ev}}$  value for  $T > 190$  K. However, the large value  $E_a^{\text{ev}} = 10.2$  kcal/mol of Delval and Rossi<sup>42</sup> is balanced by a correspondingly smaller negative activation energy for adsorption,  $E_a^c = -1.5$  kcal/mol, to result in an enthalpy of sublimation identical to that obtained in this work as displayed in Tables 4, 5, and 6. The enthalpy of sublimation of  $H_2O(\text{ice})$  from ice,  $\Delta H_S^\circ$ , is given by the difference in the activation energy for evaporation and condensation,  $E_a^{\text{ev}} - E_a^c$ . As displayed in Table 6, the value of  $\Delta H_S^\circ$  for C<sub>2</sub> ice for the high- and the low-temperature regime is equal to  $12.0 \pm 2.6$  and  $12.1 \pm 1.5$  kcal/mol, for  $T > 190$  and  $T < 190$  K, respectively, which is in excellent agreement with the accepted literature value for ice<sup>47</sup> of 12.2 kcal/mol. Moreover, Delval and Rossi<sup>42</sup> obtained  $12.3 \pm 0.5$  and  $11.7 \pm 0.6$  kcal/mol below and above 193 K, respectively, while Fraser et al.<sup>45</sup> obtained  $\Delta H_S^\circ = E_a^{\text{ev}} = 11.5$  kcal/mol for  $T < 193$  K. This latter low value for  $\Delta H_S^\circ$  may in part be explained by the fact that  $E_a^c$  was arbitrarily set to zero. Fortunately, this assumption does not have a large effect on  $\Delta H_S^\circ$  in the low  $T$  range where only a small negative value for  $E_a^c$  is observed. The present results clearly demonstrate that the assumption  $E_a^c = 0$  at  $T > 190$  K would clearly lead to an erroneous, that is lower, value

of  $\Delta H_S^\circ$  in that  $T$  range in comparison with the accepted literature values. This work is in agreement with the results of Delval and Rossi<sup>42</sup> who claimed that the sole measurement of  $E_a^{\text{ev}}$  in general is not sufficient for the determination of  $\Delta H_S^\circ$  in conjunction with the assumption  $E_a^c = 0$ . Haynes et al.<sup>40</sup> and Davy and Somorjai<sup>1</sup> obtained  $11.8 \pm 0.2$  and  $12.2$  kcal/mol for  $\Delta H_S^\circ$  of  $H_2O(\text{ice})$  ice, respectively, both of which are in agreement with the accepted literature value of Jancso et al.<sup>47</sup> Sack and Baragiola<sup>46</sup> who also assumed  $E_a^c = 0$  and obtained 0.45 eV/molecule which corresponds to  $10.3 \pm 0.7$  kcal/mol at  $T < 190$  K is significantly lower than the accepted literature value. The kinetic and thermodynamic parameters for  $E_a^c$ ,  $E_a^{\text{ev}}$ , and  $\Delta H_S^\circ$  are all displayed in Tables 4–6, respectively, to summarize and facilitate a critical comparison. The entropy of sublimation for C<sub>2</sub> ice was  $\Delta S_S = 34.6 \pm 2.5$  cal K<sup>-1</sup> mol<sup>-1</sup>, which is in fair agreement with the value of 31.0 cal K<sup>-1</sup> mol<sup>-1</sup> measured by Haynes et al.<sup>40</sup>

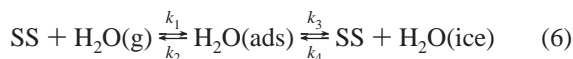
### 3.8. Thermochemical Parameters for Other Types of Ice.

The energies of activation  $E_a^c$  and  $E_a^{\text{ev}}$  for the other investigated types of ice have been obtained from the  $T$  dependence of  $J_{\text{ev}}$  and  $k_c$  and are listed in Tables 4–6 together with  $T_{\text{break}}$ , the temperature of transition in the Arrhenius plot of  $\ln k_c$  or  $\ln J_{\text{ev}}$  vs  $1000/T$ . Taking B ice as an example, we obtained  $E_a^c = -2.3 \pm 0.9$  and  $-0.24 \pm 0.11$  kcal/mol in the range 185–210 K and in the range 160–185 K, respectively. The enthalpy of sublimation  $\Delta H_S^\circ$  for B ice is identical to that of C<sub>2</sub> ice within experimental uncertainty with  $\Delta H_S^\circ = 12.2 \pm 1.7$  kcal/mol for  $\gamma$  values at  $T > 185$  K and  $\Delta H_S^\circ = 11.8 \pm 1.1$  kcal/mol at  $T < 185$  K. Chaix et al.<sup>38</sup> obtained  $12.5 \pm 2.7$  for the high-

temperature regime and  $12.5 \pm 0.6$  kcal/mol for the low-temperature regime (Table 6) with  $T_{\text{break}}$  measured at 190 K for  $\Delta H_S^\circ$  on D<sub>2</sub><sup>16</sup>O(ice) B ice. The kinetic parameters ( $E_a^c$ ,  $E_a^{\text{ev}}$ ) of Chaix et al.<sup>38</sup> are remarkably similar to the present values as displayed in Tables 4 and 5 including the value of  $T_{\text{break}} = 190$  K for C<sub>2</sub> ice.

For a large H<sub>2</sub>O(g) dose interacting with SC ice  $E_a^c = -3.1 \pm 0.6$ ,  $E_a^{\text{ev}} = 8.5 \pm 0.5$  kcal/mol in the range 170–205 K whereas  $E_a^c = -0.26 \pm 0.15$ ,  $E_a^{\text{ev}} = 11.6 \pm 0.8$  kcal/mol was measured between 145 and 170 K as displayed in Tables 4 and 5. For the medium and small doses of H<sub>2</sub>O(g) interacting with SC ice, the temperature range is not sufficiently large to draw conclusions on the location of  $T_{\text{break}}$ . The related energy of sublimation  $\Delta H_S^\circ$  for the large H<sub>2</sub>O(g) dose is equal to  $11.6 \pm 1.1$  kcal/mol in the high-temperature range  $T > 170$  K and to  $11.9 \pm 1.0$  kcal/mol in the low-temperature range  $T < 170$  K.  $\Delta H_S^\circ$  was calculated as  $12.3 \pm 1.6$  kcal/mol for the medium dose on SC ice obtained across the full  $T$  range. Because  $E_a^c$  is close to zero on S ice, namely,  $-0.3 \pm 0.2$  kcal/mol,  $E_a^{\text{ev}}$  must be close to  $\Delta H_S^\circ$ , which we evaluated as  $E_a^{\text{ev}} = 11.5 \pm 0.6$  leading to  $\Delta H_S^\circ = 11.8 \pm 0.8$  kcal/mol. This value is in agreement with  $\Delta H_S^\circ$  calculated for C<sub>2</sub>, B, and SC ice within the uncertainty of the measurement. The results of Table 6 reveal that  $\Delta H_S^\circ$  is identical within the uncertainty of the data for the different types of ice. We also found that for C, B, and SC ice there is a discontinuity in the Arrhenius plot of  $k_c$  or  $\gamma$  at  $T_{\text{break}}$ . However,  $T_{\text{break}}$  does not occur at the same temperature for the three mentioned types of ice. This may be explained by the fact that the change in the rate-limiting step in the precursor mechanism is a function of the type of ice.

To interpret the condensation of H<sub>2</sub>O(g) on ice, we use the Langmuir ansatz expressed in reaction 6<sup>38</sup>



where SS is a free surface site. H<sub>2</sub>O(ads) and H<sub>2</sub>O(ice) correspond to the precursor species responsible for the negative temperature dependence of  $k_c$  or  $\gamma$  and the thermodynamically stable bulk I<sub>h</sub> ice H<sub>2</sub>O(ice), respectively.

Results from chemical-kinetic modeling<sup>38,39</sup> indicate that  $k_1$  depends on the type of ice whereas the values  $k_2$ ,  $k_3$ , and  $k_4$  strongly depend on  $T$  but not on the type of ice. By use of the enthalpy diagram of Flückiger et al.<sup>39</sup> for the present case of H<sub>2</sub>O(g) adsorption,  $k_3$  is rate-limiting for H<sub>2</sub>O(g) uptake on ice at  $T < T_{\text{break}}$ , that is,  $k_3 < k_2$  and H<sub>2</sub>O desorption from H<sub>2</sub>O(ads) is not important at these low temperatures. At  $T \geq T_{\text{break}}$ ,  $k_2$  increasingly becomes larger than  $k_3$  so that the desorption of H<sub>2</sub>O(ads) from the precursor state  $k_2$  is faster compared to rearrangement of H<sub>2</sub>O(ads) into H<sub>2</sub>O(ice), process 3. Conversely,  $J_{\text{ev}}$  at  $T < T_{\text{break}}$  is controlled by  $k_4$ , that is,  $k_4[\text{SS}] \ll k_2$ , whereas for  $T \geq T_{\text{break}}$   $k_3$  significantly increases such that a fraction of H<sub>2</sub>O(ads) predestined for evaporation in process 2 returns to H<sub>2</sub>O(ice) via rearrangement process 3. The non-Arrhenius behavior of both  $k_c$  and  $J_{\text{ev}}(R_{\text{ev}})$  displayed in Figure 11 is thus rooted in the unequal  $T$  dependences of the rate coefficients  $k_1$  to  $k_4$ .

In fact, Tables 4 and 5 show that the individual values of  $T_{\text{break}}$  for both  $J_{\text{ev}}$  and  $k_c$  coincide within experimental uncertainty. This is a necessary requirement for the thermochemical closure of the condensation/evaporation kinetics discussed below.

**3.9. The Equilibrium Vapor Pressure  $P_{\text{eq}}$  as a Thermodynamic Constraint for Chemical Kinetics.** We have calculated the vapor pressure  $P_{\text{eq}}$  of water vapor in equilibrium with

water ice using both  $J_{\text{ev}}$  or  $R_{\text{ev}}$  and  $k_c$ , which were separately determined for the different types of ice as explained in the previous sections. The measured equilibrium vapor pressure  $P_{\text{eq}}$  is calculated using eq 7 in order to check if the different types of ice (C, B, SC, and S) significantly differ in  $P_{\text{eq}}$  at a given temperature. The calculation of  $P_{\text{eq}}$  makes use of the measured value of  $k_c$ ,  $F_{\text{ev}}$ , and  $T_S$ , the temperature of the ice substrate, and serves as a powerful thermodynamic constraint for the internal consistency of the measured kinetic parameters.

$$P_{\text{eq}} = \frac{F_{\text{ev}}RT_S}{k_cV} [\text{Torr}] \quad (7)$$

Because the sample and the reactor temperature are different,  $k_c$  has been corrected for this temperature difference as shown by Delval and Rossi.<sup>34</sup> As an example for the magnitude of this correction, one obtains  $P_{\text{eq}}$  values smaller by 23 and 18% at 180 and 200 K, respectively, using the corrected  $k_c$  in eq 7 compared to the uncorrected one. To observe a trend in the equilibrium vapor pressure for the different types of ice,  $P_{\text{eq}}$  was plotted as a function of  $T$  in Figure 12 using data from Tables ESI-1 to ESI-7 that exhibit the complete data for  $J_{\text{ev}}$  and  $P_{\text{eq}}$ .

Most  $P_{\text{eq}}$  values are comprised in the stated uncertainty range according to the  $1/e$  criterion. The largest deviation at the end of the low  $T$  measurement range is approximately 100% at  $T = 150$  K for B ice, which is the lowest value of  $P_{\text{eq}}$  that could be measured. We conclude that the  $P_{\text{eq}}$  values are identical for all the different types of ice investigated despite the individual differences in  $R_{\text{ev}}$  and  $k_c$  values. Both will change to the same extent in order to keep  $[\text{H}_2\text{O}(\text{g})]_{\text{eq}}$  or  $P_{\text{eq}}$  constant at a given  $T$  for all ices. The present results indicate that  $P_{\text{eq}}$  measured in the present work is in general larger by a factor of  $1.83 \pm 0.20$  in comparison to the results of Haynes et al.<sup>40</sup> As an example, they obtained  $P_{\text{eq}} = 6.0 \times 10^{-6}$  Torr at 175 K while the present work leads to  $P_{\text{eq}} = 1.1 \times 10^{-5}$  Torr for C<sub>1</sub> ice. According to eq 7, this is consistent with the fact that  $J_{\text{ev}}$  of Haynes et al.<sup>40</sup> is identical to the present work whereas their  $\gamma$  (or  $k_c$ ) value ( $\gamma = 0.67$  at 175 K) is larger by a factor of 1.76 in comparison to the present work.

The full and dashed lines drawn in Figure 12 represent  $P_{\text{eq}}$  given by Marti and Mauersberger<sup>43</sup> between 169 and 240 K and by Mauersberger and Krankowsky<sup>48</sup> in the range 164.5–169 K, respectively.  $P_{\text{eq}}$  values from these two references seem to be larger compared to those measured in this work by approximately 50%. This difference is consistent within the uncertainty of the present results as displayed by the typical uncertainty limits given in Figure 12. We therefore conclude that our  $P_{\text{eq}}$  values are identical to those measured by Mauersberger and co-workers within the stated uncertainty limits.

#### 4. Atmospheric Implications and Conclusions

The measured  $\gamma$  values for  $T > 205$  K displayed for C ice in Figures 3 and 5 are found to be systematically low compared to values obtained using a stirred flow reactor where the partial pressure of H<sub>2</sub>O(g) is larger compared to results obtained under molecular flow conditions such as used in this work.<sup>42</sup> The  $\gamma$  values for D<sub>2</sub><sup>18</sup>O(g) vapor interacting with D<sub>2</sub><sup>16</sup>O(ice) ice obtained by Chaix et al.<sup>38</sup> also dropped precipitously in the range 205–219 K to result in a systematic low bias. In contrast, the above-referenced  $\gamma$  values of Delval and Rossi<sup>42</sup> extend up to 240 K without extensive decrease at the high  $T$  end. It seems plausible to attribute this drooping of  $\gamma$  obtained in the present

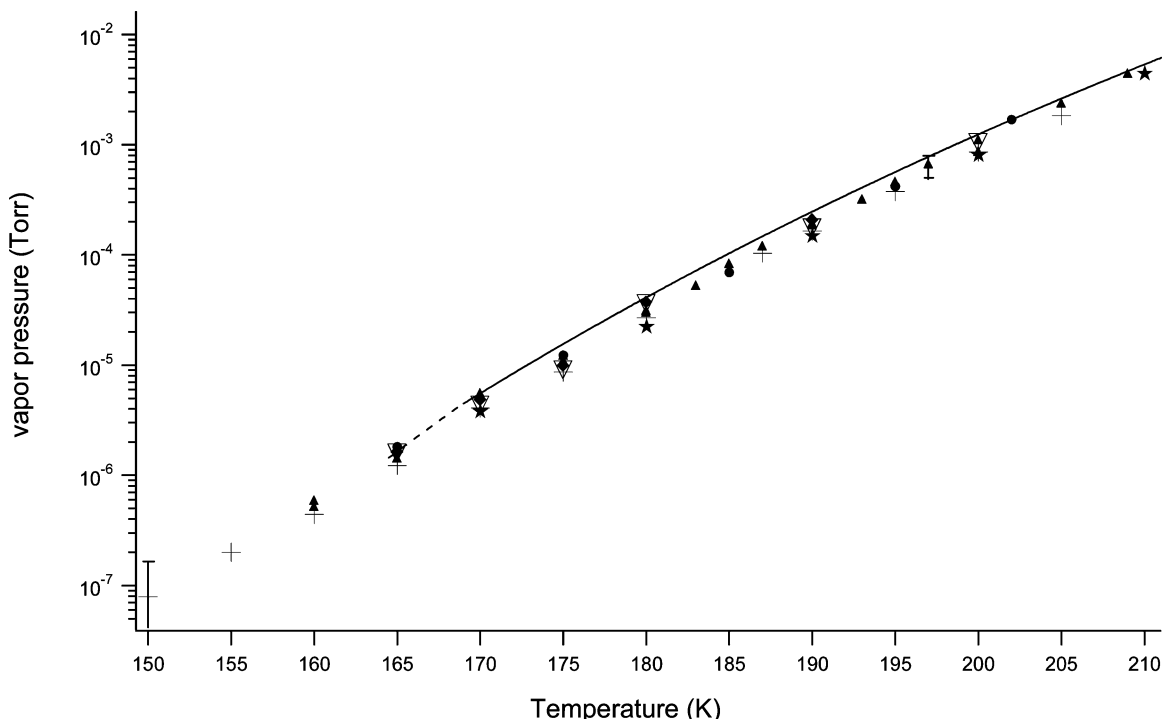


**Figure 12.** Equilibrium  $\text{H}_2\text{O}(\text{g})$  vapor pressure  $P_{\text{eq}}$  measured using forward and backward rates obtained from the PV technique for difference types of ice. Data labeled ( $\blacktriangle$ ), ( $+$ ), ( $\blacklozenge$ ), ( $\blacktriangledown$ ), and ( $\bullet$ ) correspond to C, B, SC (large dose), SC (medium dose), and S ice, respectively. The ( $\star$ ) symbol represents  $P_{\text{eq}}$  measured by the CFM experiment (Appendix A). The full and the dashed lines represent the results of Marti and Mauersberger<sup>43</sup> and Mauersberger and Krankowsky,<sup>48</sup> respectively. The uncertainty displayed at 197 K serves as an illustration of the typical uncertainty.

study under molecular flow conditions to an unexpected change of the evaporation rather than to the condensation rate. It appears that the evaporation rate or flux,  $R_{\text{ev}}$  or  $J_{\text{ev}}$ , unduly increases with temperature above 205 K thereby effectively decreasing the measured  $\gamma$  value despite our ability to separate both rate processes. Because this effect takes place at the high-temperature end of the range corresponding to a reduced surface residence time compared to the low-temperature end, we attribute this increase in  $J_{\text{ev}}$  to possible incomplete energy accommodation of the  $\text{H}_2\text{O}$ –ice adsorbate or precursor state on the ice surface. One has to remember that in the present experiment  $\text{H}_2\text{O}(\text{g})$  vapor at ambient temperature collides with an ice surface at a given low  $T$  and that energy accommodation must occur prior to evaporation. This incomplete thermalization process of the  $\text{H}_2\text{O}(\text{ads})$  precursor state on the surface may be compared to chemical activation for gas-phase processes. Because Delval and Rossi<sup>42</sup> performed their study at higher total pressure, corresponding to stirred flow conditions, the degree of thermalization of the adsorbed  $\text{H}_2\text{O}(\text{ads})$  precursor is expected to be higher on account of the increased number of collisions.

The time,  $t_{\text{ev}}$ , to complete evaporation of an ice particle of radius  $r$  at a given relative humidity (RH) is given in eq 8

$$t_{\text{ev}} = \frac{\left(\frac{\rho N_{\text{L}}}{M}\right)^{2/3} \left(\frac{r}{a}\right)}{J_{\text{ev}}(1 - \text{RH})} \quad (8)$$

where  $\rho$  is the density of ice,  $M = 18 \text{ g mol}^{-1}$  for  $\text{H}_2\text{O}$ ,  $r$  is the ice particle radius, and  $a$  is the distance between two layers of  $\text{H}_2\text{O}(\text{ice})$  in ice.<sup>20</sup> Equation 8 is based on layer-by-layer evaporation of  $\text{H}_2\text{O}(\text{ice})$  of a spherical ice particle following a zero-order rate law. For  $\text{RH} = 80\%$ ,  $J_{\text{ev}} = 10^{17} \text{ molecules s}^{-1} \text{ cm}^{-2}$ , and  $a = 4 \times 10^{-8} \text{ cm}$ , we obtain  $t_{\text{ev}} = 125 \text{ s}$ , which is a lower limit to the true evaporation time owing to the competition of mass transfer and heterogeneous chemistry whose

rate constants  $k_{\text{diff}}$  and  $k_{\text{c}}$  are given in eqs 9 and 10

$$k_{\text{diff}} = 4\pi r_0 D N_0 \quad (9)$$

$$k_{\text{c}} = \frac{\bar{c}}{4} \gamma (S/V) \quad (10)$$

$D$ ,  $N$ , and  $(S/V)$  correspond to the diffusion coefficient of  $\text{H}_2\text{O}(\text{g})/\text{atmosphere}$  of air ( $\sim 0.1 \text{ cm}^2 \text{ s}^{-1}$ ),  $N$  to the ice particle number density (particles  $\text{cm}^{-3}$ ), and  $(S/V)$  to the surface area density ( $\text{cm}^2 \text{ cm}^{-3}$ ) using  $N_0 4\pi r_0^2 = (S/V)$  as a constraining condition.

The overall rate constant  $k_{\text{tot}} = k_{\text{c}} k_{\text{diff}} / (k_{\text{c}} + k_{\text{diff}})$  is calculated to be  $7.1 \times 10^{-4} \text{ s}^{-1}$  with  $k_{\text{diff}} = 1.0 \times 10^{-3} \text{ s}^{-1}$  and  $k_{\text{c}} = 2.4 \times 10^{-3} \text{ s}^{-1}$  using  $(S/V) = 10^{-6} \text{ cm}^2 \text{ cm}^{-3}$  and  $r = 1 \text{ }\mu\text{m}$ . Thermodynamic closure requires that both  $k_{\text{c}}$  and  $J_{\text{ev}}$  are slowed by diffusion to the same extent. This leads to a factor of  $2.4 \times 10^{-3} / 7.1 \times 10^{-4} = 3.4$  by which  $J_{\text{ev}}$  is slowed at atmospheric pressure compared to molecular flow conditions. This leads to an improved estimate for  $t_{\text{ev}}$  of 425 s or approximately 7 min. It behooves us to point out that  $t_{\text{ev}}$  for large ice particles is entirely characterized by gas-phase diffusion of  $\text{H}_2\text{O}(\text{g})$  toward the ice particle and that therefore the overall rate constant  $k_{\text{tot}}$  is only marginally affected by  $k_{\text{c}}$  or  $\gamma$ .

The four messages resulting from this work that are important for atmospheric applications are the following:

(a) The uptake coefficient  $\gamma$  is significantly less than unity for  $T > 130 \text{ K}$ . This decrease compared to the theoretical maximum amounts to approximately an order of magnitude for C ice at 200 K. The identical decrease applies also for the corresponding  $J_{\text{ev}}$  values compared to their theoretical maximum value  $J_{\text{ev}}^{\text{max}}$  owing to thermochemical constraints. The largest  $\gamma$  value was measured on K ice at 130 K and led to  $\gamma = 0.64 \pm 0.05$ . For B and C ice,  $\gamma$  ranged from  $0.35 \pm 0.02$  to  $0.10 \pm 0.02$  and  $0.48 \pm 0.04$  to  $0.08 \pm 0.03$  in the range 140–210 K, respectively. On S ice  $\gamma$  is between  $0.32 \pm 0.05$  and  $0.29 \pm$

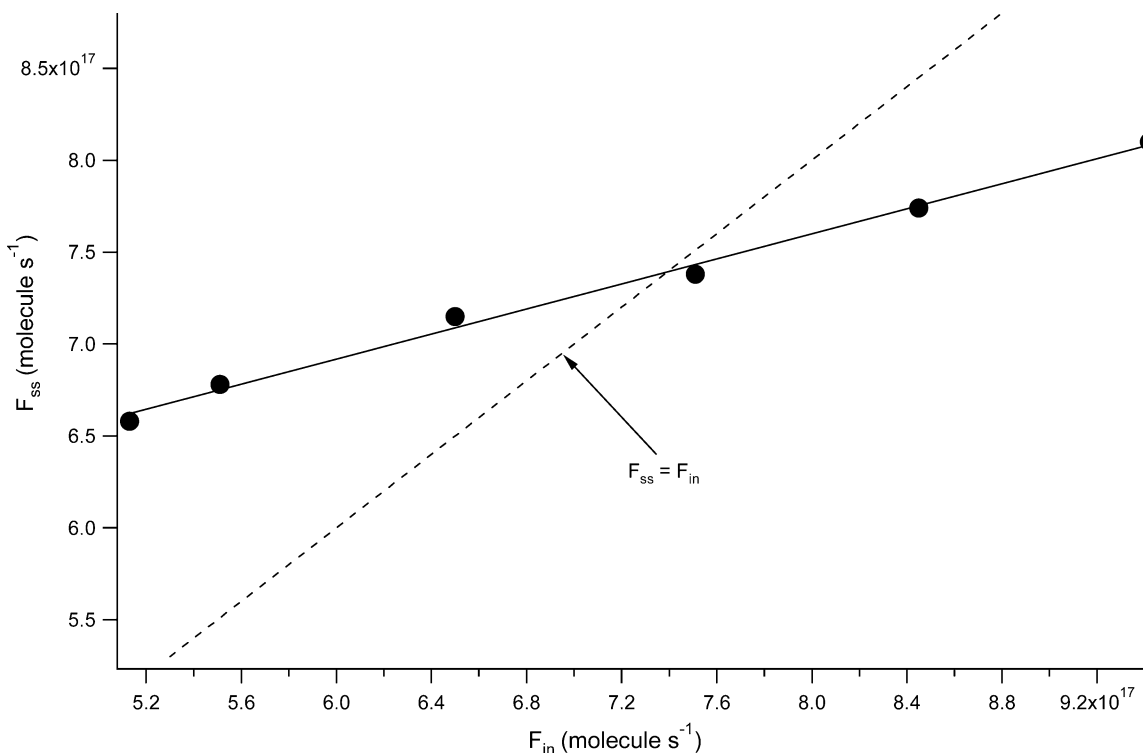


**Figure 13.**  $F_{ss}$  as a function of  $F_{in}$  in the measurement of  $J_{ev}$  and  $k_c$  for B ice at 200 K using the 14 mm aperture.

0.02 in the range 136–200 K while for SC ice  $\gamma$  lies between  $0.38 \pm 0.01$  and  $0.057 \pm 0.007$  in the range 145–205 K.

(b) The kinetic parameters ( $J_{ev}$ ,  $k_c$ ) depend on the type of ice for each type of ice investigated whereas the thermodynamic parameters ( $\Delta H_{sub}^\circ$ ,  $\Delta S_{sub}$ ) are independent of the type of ice within experimental uncertainty.

(c) The molecular mechanism for adsorption/desorption of H<sub>2</sub>O(g) vapor over ice is complex as evident from the negative temperature dependence of  $k_c$ . In contrast to previous work, additional details have been discovered in terms of a change in slope in both  $k_c(T)$  and  $J_{ev}(T)$  when  $k_c$  is represented in Arrhenius form. This “break” in slope occurs in the range  $(170–190) \pm 5$  K depending on the type of ice and is related to the fact that the relative importance of  $k_2$  and  $k_3$  in the detailed chemical kinetic mechanism is increasing with increasing  $T$ .

(d) The rate of adsorption  $k_1$  in the complex mechanism depends on the defect structure or, more generally, on structural parameters of the ice sample. The colliding H<sub>2</sub>O(g) molecule has to search for an active site on the ice to enable the formation of the precursor state consistent with Langmuir ansatz. Therefore,  $k_1$  depends on the type of ice whereas the remaining parameters  $k_2$ ,  $k_3$ , and  $k_4$  do not within the uncertainty of the data. However, the latter rate constants strongly depend on  $T$  in contrast to  $k_1$ .

In conclusion, the kinetic data collected in this investigation should encourage workers in the field to obtain well-characterized atmospheric ice samples that may be compared to the surrogate ices investigated in the present study.

**Acknowledgment.** Generous support of this research was granted by OFES (Office Fédéral de l’enseignement et de la science) in the framework of the EU projects CUTICE and THALOS.

## Appendix A

**Additional Experiments. CFM and TASSM: Two Alternative Steady-State Experiments.** To measure  $J_{ev}$ , we have

used two additional, albeit different steady-state methods, namely, the compensated flow method (CFM) and the two-aperture steady-state method (TASSM) with the goal to compare results of both  $k_c$  and  $J_{ev}$  obtained from steady-state and transient (PV) methods. B ice samples have been used for the confirmation of the present PV results on  $J_{ev}$  displayed in Figure 9 and Table ESI-6.

The general way to perform a CFM experiment is to measure the H<sub>2</sub>O(g) flow,  $F_{ss} = V[\text{H}_2\text{O}]k_{esc}$ , escaping from the flow reactor as a function of an additional measured H<sub>2</sub>O(g) flow, namely,  $F_{in}$ , in the presence of ice. The mass balance is expressed in eq A-1 which leads to eq A-2 after rearrangement

$$F_{in} + F_{ev} = F_{ss} + V[\text{H}_2\text{O}(g)]k_c \quad (\text{A-1})$$

$$F_{ss} = \frac{F_{ev}}{1 + \frac{k_c}{k_{esc}}} + \frac{F_{in}}{1 + \frac{k_c}{k_{esc}}} \quad (\text{A-2})$$

where  $F_{ev}/(1 + (k_c/k_{esc}))$  and  $1/(1 + (k_c/k_{esc}))$  are the intercept and slope of the straight line of a plot of  $F_{ss}(F_{in})$ , respectively.

For the special case of  $F_{in} = F_{ss}$ ,  $J_{ev}$  may be evaluated from eq A-3

$$J_{ev} = \frac{F_{ev}}{A_s} = \frac{k_c}{k_{esc}} \frac{F_{ss}}{A_s} \quad (\text{A-3})$$

In this case the flow rate  $F_{in}$  is chosen in such a way so as to exactly match  $F_{ss}$ , in the presence of the ice sample. To calculate  $J_{ev}$  using eq A-3, we use  $k_c$  measured on B ice using a PV experiment (Table ESI-2). All CFM data on H<sub>2</sub>O interacting with B ice are summarized in Table ESI-6.

A more general approach to measure both  $J_{ev}$  and  $k_c$  is to plot  $F_{ss}$  as a function of  $F_{in}$  and dividing the intercept by the slope of the straight line expressed in eq A-2. An example of such a plot is shown in Figure 13 where the measurement was performed on B ice held at 200 K. In a PV experiment  $F_{ev}$  was

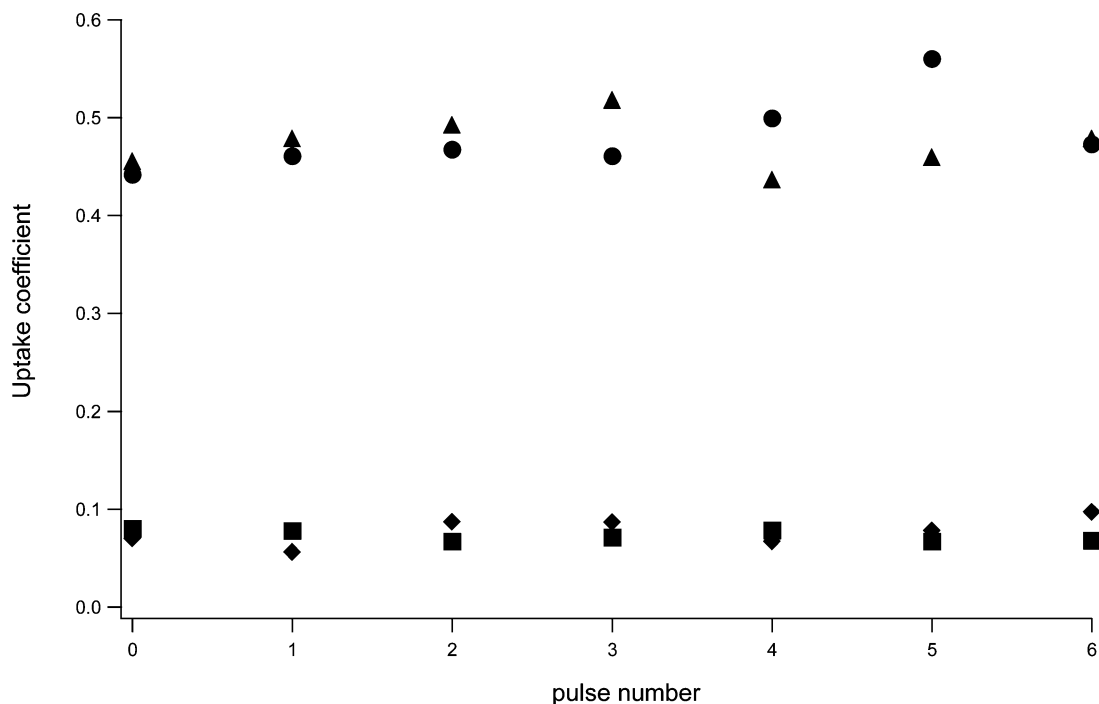


**Figure 14.** Repetitive pulse experiment (RPE) on  $C_2$  ice. The uptake coefficient  $\gamma$  is plotted as a function of the pulse event for different pulse frequencies and temperature. The ( $\blacktriangle$ ) and the ( $\bullet$ ) data points were obtained at 170 K at frequencies of 1 and 3 Hz, respectively. The ( $\blacksquare$ ) and the ( $\blacklozenge$ ) results were obtained at 210 K at frequencies of 1 and 3 Hz, respectively. The dose used to measure  $\gamma$  was  $5.0 \times 10^{16}$  molecules/pulse.

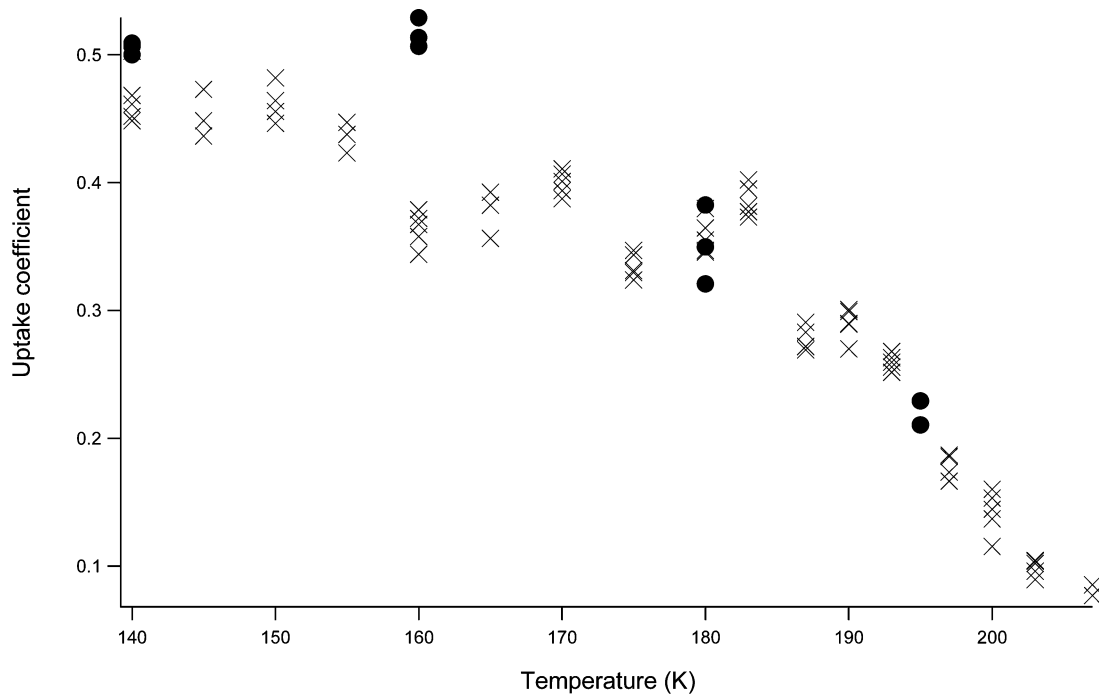


**Figure 15.** Uptake coefficient  $\gamma$  on  $C_1$  ice for fresh ( $\times$ ) and annealed ( $\bullet$ ) ice as a function of  $T$ . The ice surface was annealed at 220 K for 10 min prior to the PV measurement.

calculated to be  $1.4 \times 10^{18}$  molecules  $s^{-1}$  leading to  $J_{ev} = (7.9 \pm 1.1) \times 10^{16}$  molecules  $cm^{-2} s^{-1}$  and  $k_c = 13.8 \pm 1.7 s^{-1}$ . The knowledge of both the slope and intercept of the straight line  $F_{ss}(F_{in})$  leads to the separate determination of  $F_{ev}$  or  $J_{ev}$  and  $k_c$ , namely,  $J_{ev} = (6.8 \pm 1.9) \times 10^{16}$  molecules  $cm^{-2} s^{-1}$  and  $k_c = 16.3 \pm 4.1 s^{-1}$ . We conclude that the PV and CFM experiments are in good agreement within experimental uncertainty. For all results displayed in Table ESI-6, the kinetics was calculated by using eq A-3 ( $F_{in} = F_{out}$ ) where  $F_{in} = F_{ss}$  was chosen by trial and error for B ice at 200 K.

The second technique, TASSM, uses two or more independent data sets of  $F_{ss}$  and  $k_{esc}$  by choosing two or more escape apertures (14 and 8 mm) and measuring the corresponding value of  $F_{ss}$ . Using eq 4, we obtain two independent sets of equations to be solved for  $F_{ev}$  and  $k_c$ . The solution for  $F_{ev}$  and  $k_c$  is given in eq A-4

$$F_{ev} = \frac{F_{ss}(L)(k_{esc}(L) - k_{esc}(S))}{k_{esc}(L) - rk_{esc}(S)} \quad (A-4)$$

and

$$k_c = \frac{(r-1)k_{\text{esc}}(S)k_{\text{esc}}(L)}{k_{\text{esc}}(L) - rk_{\text{esc}}(S)}$$

with

$$r = F_{\text{ss}}(L)/F_{\text{ss}}(S)$$

where  $L$  and  $S$  are related to the large ( $L$ ) and small ( $S$ ) escape aperture, respectively.

By measuring  $F_{\text{ss}}(L)$ ,  $F_{\text{ss}}(S)$ , at known values of  $k_{\text{esc}}(L)$  and  $k_{\text{esc}}(S)$  for B ice at different temperatures, we obtain  $F_{\text{ev}}$  and  $k_c$ . All experimental data for TASSM are summarized in Table ESI-7. Unfortunately, this method is more sensitive to experimental uncertainties due to the subtraction of two similar values in the denominator as may be seen from eq A-4. This leads to a large uncertainty for both  $k_c$  and  $F_{\text{ev}}$ .

To show that a PV experiment of H<sub>2</sub>O vapor interacting with ice does not affect  $J_{\text{ev}}$  in the aftermath of a H<sub>2</sub>O(g) pulse, both CFM and TASSM experiments have been performed on B ice as both are essentially steady-state experiments.  $J_{\text{ev}}$  on B (▼) ice using CFM matched that measured using the PV (×) technique, within 15%, except for 175 K and is displayed in Figure 9.

In addition, we have performed repetitive pulse experiments (RPEs) of H<sub>2</sub>O(g) interacting with C<sub>2</sub> ice at 170 and at 210 K at different pulse frequencies in order to test if  $k_c$  changes on the time scale of the present experiments or if there are measurable memory effects on the ice substrate originating from previous probe pulses. We have summarized the results of this experiment in Figure 14 where  $\gamma$  is plotted as a function of the number of pulse events, at two temperatures and pulse frequencies using a dose of  $5 \times 10^{16}$  molecules/pulse. These experiments tell us that the pulse decay rate constant is independent of the number of previous pulses and therefore does not affect the measured kinetics at low and high temperature. We conclude that there is no measurable difference at both 210 and 170 K for the two chosen pulse frequencies of 1 and 3 s<sup>-1</sup>. Similarly, Haynes et al.<sup>40</sup> concluded that an additional flow of H<sub>2</sub>O(g) perturbs neither the evaporation nor the condensation of H<sub>2</sub>O(g) on ice.

## Appendix B

To ascertain that C ice preserves the hexagonal I<sub>h</sub> ice structure under annealing, we first deposited C<sub>1</sub> ice at  $T = 180$  K, which is under conditions that result in the formation of ice with I<sub>h</sub> structure, cooled it subsequently to 140 K, and measured  $k_c$  using the PV technique. By increasing the annealing temperature and measuring  $\gamma$ , we obtain the kinetic data with the (×) label of Figure 15. We annealed the surface to 220 K for 10 min before lowering it to 140 K in order to perform a second set of measurements labeled with the (●) symbol. In Figure 15, the crosses and the circle symbols therefore describe the  $\gamma$  values measured before and after annealing to 220 K, respectively. Before each temperature change, 10 min was allowed before performing measurement to obtain ice temperature homogeneity. The first  $\gamma$  was measured at 140 K (×) while  $T$  was increased sequentially to reach 209 K after approximately 160 min. After the annealing at 220 K,  $T$  was decreased at 140 K and  $\gamma(T)$  was measured subsequently at 140, 160, 180, and 195 K in 40 min. There is no significant difference between  $k_c$  obtained before and after the annealing process for hexagonal C ice I<sub>h</sub> for the duration of the experiment (over 200 min) as displayed

in Figure 15.<sup>36,38</sup> This leads to the conclusion that the non-Arrhenius behavior of  $k_c$  at  $T_{\text{break}}$  is related to the chemical-kinetic mechanism displayed in reaction 6 as opposed to a phase transition.

**Supporting Information Available:** Tables of condensation rate constants, evaporation rates, and equilibrium vapor pressures for C<sub>2</sub>, B, SC, and S ice and figure showing uptake coefficient of H<sub>2</sub>O(g) as a function of temperature. This material is available free of charge via the Internet at <http://pubs.acs.org>.

## References and Notes

- (1) Davy, J. G.; Somorjai, G. A. *J. Chem. Phys.* **1971**, *55*, 3624.
- (2) Intergovernmental Panel on Climate Change (IPCC). [http://www.grida.no/climate/ipcc\\_tar/](http://www.grida.no/climate/ipcc_tar/).
- (3) Shaw, R. A. *J. Atmos. Sci.* **2000**, *57*, 3452.
- (4) Spichtinger, P.; Gierens, K.; Smit, H. G. J.; Ovarlez, J.; Gayet, J. *F. Atmos. Chem. Phys.* **2004**, *4*, 639.
- (5) Shine, K. P.; Sinha, A. *Nature* **1991**, *354*, 382.
- (6) Jensen, E. J.; Toon, O. B.; Vay, S. A.; Ovarlez, J.; May, R.; Bui, T. P.; Twohy, C. H.; Gandrud, B. W.; Pueschel, R. F.; Schumann, U. *J. Geophys. Res.*, [Atmos.] **2001**, *106*, 17253.
- (7) Gierens, K.; Brinkop, S. *Theor. Appl. Climatol.* **2002**, *71*, 129.
- (8) Gierens, K.; Spichtinger, P. *Ann. Geophys.* **2000**, *18*, 499.
- (9) Gibson, G. G.; Wielicki, B. A. *CERES Interdisciplinary Science Principal Investigator, NASA Langley Research Center (LaRC)*, <http://asd-www.larc.nasa.gov/ceres/ASDCeres.html>.
- (10) Gierens, K.; Schumann, U.; Helten, M.; Smit, H.; Wang, P. H. *J. Geophys. Res.*, [Atmos.] **2000**, *105*, 22743.
- (11) Penner, J. E. *Intergovernment Panel on Climate Change. Working Group I; Intergovernmental Panel on Climate Change. Working Group III. Aviation and the global atmosphere: a special report of IPCC Working Groups I and III in collaboration with the scientific Assessment Panel to the Montreal Protocol on Substances that Deplete the Ozone Layer*; Cambridge University Press: Cambridge, 1999.
- (12) Eremenko, M. N.; Zsetsky, A. Y.; Boone, C. D.; Sloan, J. J. *Geophys. Res. Lett.* **2005**, *32*.
- (13) Parungo, F. *Atmos. Res.* **1995**, *38*, 249.
- (14) Jensen, E. J.; Kinne, S.; Toon, O. B. *Geophys. Res. Lett.* **1994**, *21*, 2023.
- (15) Borrmann, S.; Solomon, S.; Dye, J. E.; Luo, B. P. *Geophys. Res. Lett.* **1996**, *23*, 2133.
- (16) Zerefos, C. S.; Eleftheratos, K.; Balis, D. S.; Zanis, P.; Tselioudis, G.; Meleti, C. *Atmos. Chem. Phys.* **2003**, *3*, 1633.
- (17) Solomon, S.; Garcia, R. R.; Rowland, F. S.; Wuebbles, D. J. *Nature* **1986**, *321*, 755.
- (18) Libbrecht, K. G. *Rep. Prog. Phys.* **2005**, *68*, 855.
- (19) Young, K. C. Oxford University Press: New York, 1993.
- (20) Hobbs, P. V. *Ice Physics*; Oxford University Press: Oxford; 1969; p 397.
- (21) Murphy, D. M. *Geophys. Res. Lett.* **2003**, *30*, DIO: 10.1029/2003GL018566.
- (22) Whalley, E. S. *Science* **1981**, *211*, 389.
- (23) Murray, J. B.; Knopf, A. D.; Bertram, K. A. *Nature* **2005**, *434*, 202.
- (24) Bonacci, J. C.; Myers, A. L.; Nongbri, G.; Eagleton, L. C. *Chem. Eng. Sci.* **1976**, *31*, 609.
- (25) Chodes, N.; Warner, J.; Gagim, A. *J. Atmos. Sci.* **1974**, *31*, 1351.
- (26) Koros, R. M.; Deckers, J. M.; Andres, R. P.; Boudart, M. *Chem. Eng. Sci.* **1966**, *21*, 941.
- (27) Kramers, H.; Stemerding, S. *Appl. Sci. Res., Sect. A* **1951**, *3*, 73.
- (28) Nabavian, K.; Bromley, L. A. *Chem. Eng. Sci.* **1963**, *18*, 651.
- (29) Isono, K.; Iwai, K. *Nature* **1969**, *223*, 1149.
- (30) Leu, M. *Geophys. Res. Lett.* **1988**, *15*, 17.
- (31) Sinarwalla, A. M.; Alofs, D. J.; Carstens, J. C. *J. Atmos. Sci.* **1975**, *32*, 592.
- (32) Schulze, F. W.; Cammenga, H. K. *Ber. Bunsen-Ges. Phys. Chem. Chem. Phys.* **1980**, *84*, 163.
- (33) Caloz, F.; Fenter, F. F.; Tabor, K. D.; Rossi, M. J. *Rev. Sci. Instrum.* **1997**, *68*, 3172.
- (34) Delval, C.; Fluckiger, B.; Rossi, M. J. *Atmos. Chem. Phys.* **2003**, *3*, 1131.
- (35) Fenter, F. F.; Caloz, F.; Rossi, M. J. *Rev. Sci. Instrum.* **1997**, *68*, 3180.
- (36) Kumai, M. *J. Glaciol.* **1967**, *7*, 95.
- (37) Knight, C. A. *J. Glaciol.* **1996**, *42*, 585.
- (38) Chaix, L.; van den Bergh, H.; Rossi, M. J. *J. Phys. Chem. A* **1998**, *102*, 10300.
- (39) Fluckiger, B.; Rossi, M. J. *J. Phys. Chem. A* **2003**, *107*, 4103.



- (40) Haynes, D. R.; Tro, N. J.; George, S. M. *J. Phys. Chem.* **1992**, *96*, 8502.
- (41) Brown, D. E.; George, S. M.; Huang, C.; Wong, E. K. L.; Rider, K. B.; Smith, R. S.; Kay, B. D. *J. Phys. Chem.* **1996**, *100*, 4988.
- (42) Delval, C.; Rossi, M. J. *Phys. Chem. Chem. Phys.* **2004**, *6*, 4665.
- (43) Marti, J.; Mauersberger, K. *Geophys. Res. Lett.* **1993**, *20*, 363.
- (44) Smith, J. A.; Livingston, F. E.; George, S. M. *J. Phys. Chem. B* **2003**, *107*, 3871.
- (45) Fraser, H. J.; Collings, M. P.; McCoustra, M. R. S.; Williams, D. A. *Mon. Not. R. Astron. Soc.* **2001**, *327*, 1165.
- (46) Sack, N. J.; Baragiola, R. A. *Phys. Rev. B* **1993**, *48*, 9973.
- (47) Jancso, G.; Pupezin, J.; Vanhook, W. A. *J. Phys. Chem.* **1970**, *74*, 2984.
- (48) Mauersberger, K.; Krankowsky, D. *Geophys. Res. Lett.* **2003**, *30*, 1121.